



Thermocapillary effects on eccentric compound drops in Poiseuille flows

Sayali N. Jadhav  and Uddipta Ghosh **Discipline of Mechanical Engineering, Indian Institute of Technology Gandhinagar,
Palaj, Gujarat 382355, India*

(Received 31 December 2020; accepted 16 June 2021; published 6 July 2021)

The dynamics of a neutrally buoyant, eccentric compound drop, suspended in a Poiseuille flow, in the presence of an external temperature gradient have been analyzed here. Assuming the energy and momentum transport to be diffusion-dominated, we derive approximate analytical solutions for the temperature and the velocity fields and subsequently deduce the deformation using asymptotic analysis in bispherical coordinates. We establish that depending on the direction, the presence of an imposed temperature gradient may speed up or slow down the drops. The temperature gradient has a stronger influence on the velocity of the inner drop at different eccentricities, which in turn alters the relative velocity between the drops. As a result, it is possible to achieve equilibrium configurations, where both the drops move with the same velocity. Two such equilibrium configurations exist for temperature gradients beyond a critical limit, one of which is stable. It is revealed that the imposed temperature gradient always increases the deformation as compared to an isothermal flow. Depending on the position of the inner core with respect to the outer drop center and the direction of the applied temperature gradient, the shape of the inner drop may change from prolate to oblate (or vice versa), as it travels within the outer drop. The deformation in the inner drop increases with eccentricity, while the outer drop sees very little deformation even for relatively large capillary numbers.

DOI: [10.1103/PhysRevFluids.6.073602](https://doi.org/10.1103/PhysRevFluids.6.073602)

I. INTRODUCTION

Compound drops or double emulsions are characterized as a single drop or multiple drops completely or partially engulfed by another drop of an immiscible fluid, itself suspended in a third immiscible continuous medium. These entities have been the subject of numerous studies over past decades, owing to their far-ranging applications in microfluidics [1,2], the food industry [3,4], the pharmaceutical industry [5,6], and biomedicine [7,8], as well as in separation processes [9]. As a result of such diverse applications, various aspects of the dynamics of compound drops have been extensively investigated [10], which include a wide spectrum of imposed background conditions, such as settling under gravity and uniform flow [11–13], deformation and breakup of compound drops in extensional and shear flows [14–17], and the impact of compound drops onto solid or liquid surfaces [18,19], to underline a few.

A review of the related literature further reveals that droplet motion and migration in parabolic and especially in Poiseuille flows has been another area of in-depth research [20–23], mainly attributable to the prevalence of such flows across various platforms [24–27]. While various aspects of motion of single drops in Poiseuille flows, with and without external effects such as electric fields [28,29], imposed temperature gradients [30,31], the presence of surface impurities [32,33], etc., have been extensively explored, thorough analyses of the motion of compound drops in Poiseuille

*uddipta.ghosh@iitgn.ac.in

flows are rather scarce and limited largely to a handful of studies [34–37]. The reason may be attributed to the fact that in Poiseuille flows, the inner and the outer drops tend to move with different velocities, giving rise to increasing eccentricity, which is mathematically extremely inconvenient to handle. As a result, many of the existing studies on compound drops [14,38–40] focus on concentric configurations.

It has long been established that a drop’s velocity and hence its trajectory can be finely tuned, by manipulating the interfacial tension [41], using Marangoni effects. In this regard, thermocapillary effects play an important role in droplet-based microfluidics [42–46], as evident from a wealth of insightful studies [45–48]. Such effects have also been demonstrated to be useful in microgravity experiments on droplets [49,50], especially where the density difference between the dispersed and the continuous phases are negligible. As such, thermocapillary migrations of double emulsions have been investigated in a handful of previous studies [38,51–54], exploring the effect of an imposed temperature gradient on migration and deformation of partially or fully engulfed compound drops, in otherwise quiescent fluids. For instance, Morton *et al.* [52] were among the first ones to analyze how an externally applied temperature gradient alters the settling of a compound drop in an unbounded medium. This was followed by studies such as thermocapillary migration of concentric compound drops in the presence of surface impurities [38], among many others [53,54]. These studies generally reveal that under the influence of a thermal gradient, the compound drop tends to migrate toward the higher temperature and when the drops are concentric, the inner drop moves faster than the outer drop.

In the case of completely engulfed compound drops, equilibrium of the core (i.e., the innermost phase), which amounts to no relative motion between the inner and the outer drops’ centers of mass, becomes especially critical when the core is used for transport of sensitive materials [4,55]. It has been previously shown [12] that by carefully choosing the density of different phases, the inner core of a settling compound drop in an otherwise quiescent surrounding medium can be stabilized. These stable equilibrium configurations lie upstream and downstream of the outer drop’s center. Later, Gouz and Sadhal [56] established that stable configurations also existed for compound drops, settling in the presence of externally imposed electric fields. Other external fields, such as imposed temperature gradients, have also been shown to be effective in generating such equilibrium configurations in settling compound drops [52]. A close review of the literature, however, reveals that a comprehensive theoretical analysis addressing the effects of an imposed temperature gradient on the movement and deformation of compound drops in Poiseuille flows still remains an open question. Such a scenario can be an effective way of transporting double emulsions, with a strong possibility of a stabilized inner core, critical for many applications.

With the above motivation in mind, here we analyze the motion and deformation of an axisymmetric neutrally buoyant compound drop, suspended in a Poiseuille flow, subject to an externally imposed temperature gradient. We consider eccentric configurations, wherein the possibilities of the inner drop center residing upstream and downstream of the outer drop center are explored separately. A bispherical coordinate system [57,58] is used to mathematically represent both the drop surfaces. Assuming the interfacial deformations to remain small, we employ asymptotic analysis to deduce the solutions for the flow variables. Our analysis reveals that the drop velocities may both increase and decrease depending on the direction and magnitude of the imposed temperature gradient, while its influence diminishes with increasing eccentricity. We further establish that the deformation of both the drops generally increases with the imposed temperature gradient, while it also strongly depends on fluid properties as well as other geometrical factors. Finally, we demonstrate that below a critical temperature gradient, two possible “equilibrium” eccentric configurations of the compound drop may be realized, one of which is stable. We establish that this constitutes an example of saddle-node bifurcation, a characteristic prevalent in many nonlinear systems [59]. We extensively validate our results for droplet velocities and deformations by comparing them with studies from the literature [30,60], as well as with the closed-form analytical solutions derived for concentric compound drops.

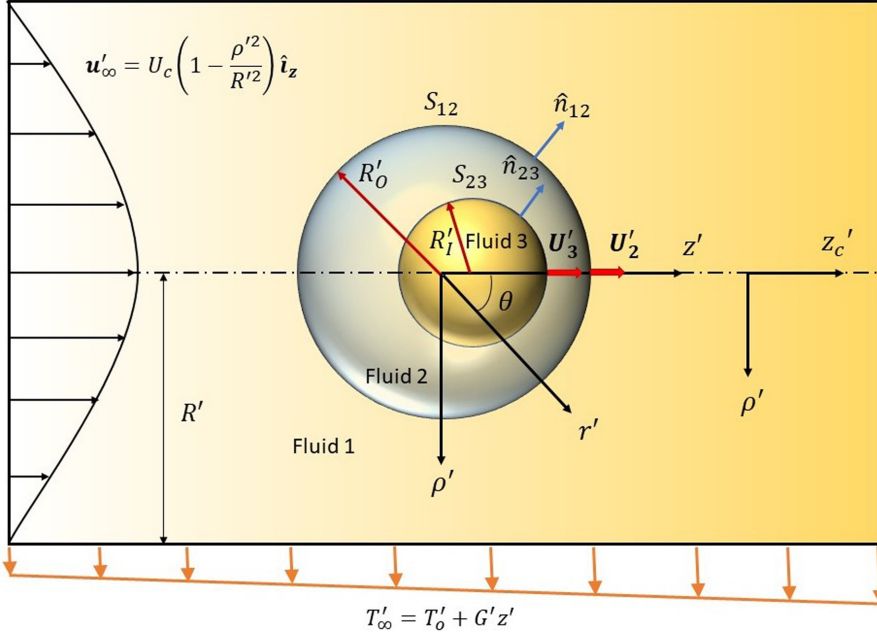


FIG. 1. Schematic of a neutrally buoyant eccentric compound drop in a Poiseuille flow (\mathbf{u}'_∞), with an imposed temperature gradient (G'). A cylindrical coordinate system (ρ' , φ , z'_c) and a spherical coordinate system (r' , θ , φ) are attached to the outer drop's center of mass. The two drops in general move with different velocities given by \mathbf{U}'_2 and \mathbf{U}'_3 for the outer and inner drop, respectively.

The rest of the paper is arranged as follows. In Sec. II, we lay out the details of the physical system under consideration, followed by Sec. III, where the governing equations and boundary conditions are discussed. In Sec. IV, asymptotic solutions for axisymmetric compound drops in bispherical coordinates have been outlined. In Sec. V, the detailed results of droplet motion and deformation are presented, and finally, we conclude in Sec. VI.

II. THE PHYSICAL PARADIGM

The system under consideration is depicted in Fig. 1. It consists of a double emulsion (e.g., oil-in-water-in-oil emulsion) suspended along the axis of a Poiseuille flow and subject to an imposed far-field temperature gradient of the form $T'_\infty = T'_0 + G'z'$, G' being the temperature gradient. Note that the dimensional variables (i.e., variables with units) here are represented with a “prime” symbol (such as z'). The outermost, intermediate, and the innermost phases are denoted by 1 (suspending medium), 2 (outer drop), and 3 (inner drop), respectively, and any property of the j th phase is denoted with a subscript j . Radii of the inner and the outer drops are R'_I and R'_O , respectively. The interface between the i th and the j th phase is denoted as S_{ij} and the corresponding unit outward normal is defined as $\hat{\mathbf{n}}_{ij} = \nabla' F'_{ij} / |\nabla' F'_{ij}|$, where F'_{ij} represents the equation of interface. The viscosity and the thermal conductivity of the i th phase are μ_i and k_i , respectively. The surface tension at the interface is denoted by γ'_{ij} . All fluid properties are assumed to be constant, except the surface tension, which varies linearly with the local temperature as [61] $\gamma'_{ij} = \gamma^{(0)}_{ij} - \beta_{ij}(T'_{ij} - T'_0)$, where $\gamma^{(0)}_{ij}$ is the surface tension at reference temperature (T'_0) and β_{ij} is the coefficient of variation of the surface tension with temperature.

An inertial cylindrical coordinate system (ρ' , z'_c , φ), moving with the outer drop's center of mass, may be set up as shown in the figure, with the z'_c axis coinciding with the axis of the imposed flow.

A spherical coordinate system (r', θ, φ) with the origin attached to the outer drop center is also shown in Fig. 1, with $z' = r' \cos \theta$ and $\rho' = r' \sin \theta$. The imposed far-field velocity is given by $\mathbf{u}'_\infty = U_c(1 - \rho'^2/R^2)\hat{\mathbf{z}}$, where U_c is the axial velocity. In a Poiseuille flow, generally the outer and the inner drops move with different velocities (here, \mathbf{U}'_2 and \mathbf{U}'_3 , respectively) [34–36] and thus in general the configuration of the drop will be eccentric, as shown in Fig. 1.

Before delving deep into the detailed mathematical formulation, it is in order to outline the key assumptions undertaken in the present study. First and foremost, the transport of momentum and energy are assumed to be diffusion-dominated, which entails [30,61] a low Péclet number ($\text{Pe} = U_c R'_O / \alpha_1 \ll 1$; α_1 is the thermal diffusivity of the suspending medium) and low Reynolds number [$\text{Re} = \rho_1 R'_O U_c / \mu_1 \ll O(1)$]. Second, although the eccentric configuration in Fig. 1 is inherently unsteady owing to the different velocities of the droplets, on account of viscosity-dominated motion, we shall assume the flow field to be quasisteady. We emphasize that this assumption has been widely used in the literature related to droplet motion [12,52,57]. Third, we shall only explore the limit of small capillary numbers [14,30] [$\text{Ca} = \mu_1 U_c / \gamma_{12}^{(0)} \ll O(1)$], which allows us to write asymptotic expansions in Ca [34] and indicates that the drops remain approximately spherical, as is generally true in viscosity-dominated flows. Finally, the drops are assumed to be neutrally buoyant; i.e., the effects of gravity and cross-migration are ignored.

III. THE GOVERNING EQUATIONS AND BOUNDARY CONDITIONS

A. The general mathematical formulation

For diffusion-dominated energy transport, neglecting viscous dissipation, the governing equations for the temperature field at steady state in the i th fluid ($i = 1, 2, 3$) are given by [30,43,61]

$$\nabla'^2 T'_i = 0. \quad (1)$$

The temperature in fluid 1 (T'_1) is subject to the following far-field condition (see Fig. 1): $T'_1 = T'_\infty = T'_0 + G'z'$ as $|\mathbf{r}'| \rightarrow \infty$ and T'_3 has to be bounded inside the inner drop, when $r' < R'_I$. The temperature and the heat flux must be continuous at the interfaces. On the interface S_{ij} , these conditions may be expressed as [30,61]

$$[T'_i]_{S_{ij}} = [T'_j]_{S_{ij}} \quad \text{and} \quad [\mathbf{q}'_i \cdot \hat{\mathbf{n}}_{ij}]_{S_{ij}} = [\mathbf{q}'_j \cdot \hat{\mathbf{n}}_{ij}]_{S_{ij}}, \quad (2)$$

where the heat flux is defined as $\mathbf{q}'_i = -k_i \nabla' T'_i$, based on Fourier's law of heat conduction [61], and $[\Xi]_{S_{ij}}$ denotes any quantity Ξ evaluated on the interface S_{ij} . For quasisteady and viscosity-dominated flows, the Stokes flow and the continuity equations for the i th fluid ($i = 1, 2, 3$) are given as [61]

$$\mu_i \nabla'^2 \mathbf{u}'_i = \nabla' p'_i, \quad \nabla' \cdot \mathbf{u}'_i = 0. \quad (3)$$

These are subject to the following far-field condition [30] (in a reference frame moving with the outer drop's center of mass): $\mathbf{u}'_1 = U_c(1 - \rho'^2/R^2)\hat{\mathbf{z}} - U'_2 \hat{\mathbf{z}}$ as $|\mathbf{r}'| \rightarrow \infty$ and \mathbf{u}'_3 and p'_3 have to be bounded inside the inner drop, when $r' < R'_I$. The boundary conditions on the interface S_{ij} are given by the following [34,61]:

$$[\mathbf{u}'_i \cdot (\mathbf{I} - \hat{\mathbf{n}}_{ij} \hat{\mathbf{n}}_{ij})]_{S_{ij}} = [\mathbf{u}'_j \cdot (\mathbf{I} - \hat{\mathbf{n}}_{ij} \hat{\mathbf{n}}_{ij})]_{S_{ij}}, \quad (4a)$$

$$[\mathbf{u}'_i \cdot \hat{\mathbf{n}}_{ij}]_{S_{ij}} = [\mathbf{u}'_j \cdot \hat{\mathbf{n}}_{ij}]_{S_{ij}} = (\mathbf{U}'_3 - \mathbf{U}'_2) \cdot \hat{\mathbf{n}}_{23} \delta_{i2} \delta_{j3}, \quad (4b)$$

$$[(\boldsymbol{\tau}'_i - \boldsymbol{\tau}'_j) \cdot \hat{\mathbf{n}}_{ij}]_{S_{ij}} = \gamma'_{ij} (\nabla' \cdot \hat{\mathbf{n}}_{ij}) \hat{\mathbf{n}}_{ij} - \nabla_s'^{(ij)} \gamma'_{ij}. \quad (4c)$$

In Eqs. (4a)–(4c), δ_{ij} represents the Kronecker delta, $\boldsymbol{\tau}'_i$ is the stress tensor in the i th fluid ($i = 1, 2, 3$), defined as $\boldsymbol{\tau}'_i = -p'_i \mathbf{I} + \mu_i [\nabla' \mathbf{u}'_i + (\nabla' \mathbf{u}'_i)^T]$, and $\nabla_s'^{(ij)}$ is the surface gradient operator on the interface, given by $\nabla_s'^{(ij)} = \nabla' - \hat{\mathbf{n}}_{ij} (\hat{\mathbf{n}}_{ij} \cdot \nabla')$. We reiterate that in all of the above equations, \mathbf{u}'_i is the velocity field in the i th fluid with respect to the outer drop's center of mass. Further recall that

the surface tension at the interface is related to the local temperature (T'_{ij}) as $\gamma'_{ij} = \gamma_{ij}^{(0)} - \beta_{ij}(T'_{ij} - T'_0)$. Finally, note that $\mathbf{U}'_2 = U'_2 \hat{\mathbf{e}}_z$ and $\mathbf{U}'_3 = U'_3 \hat{\mathbf{e}}_z$ (the outer and inner drop velocities) are *a priori* unknown, and have to be computed as part of the solution.

The above equations may be nondimensionalized by using the following characteristic scales: length, $l_c = R'_O$; velocity, $u_c = U_c$; pressure and stresses, $p_c = \tau_c = \mu_i U_c / R'_O$; surface tension, $\gamma_c = \gamma_{12}^{(0)}$; and finally characteristic heat flux, $q_c = G' k_1$. The dimensionless version of any variable, say Ξ' (such as \mathbf{u}' , p' , etc.) is expressed as $\Xi = \Xi' / \Xi_c$, where Ξ_c is the characteristic scale of the variable under consideration. The temperature field is nondimensionalized as follows: $T = (T' - T'_0) / G' R'_O$. Note that all dimensionless variables are expressed without the ‘‘prime.’’ The following dimensionless ratios may then be defined, based on the fluid properties: $R_l = R'_l / R'_O$, $\lambda_i = \mu_i / \mu_1$, $\kappa_i = k_i / k_1$, $\beta = \beta_{23} / \beta_{12}$, and $\gamma = \gamma_{23}^{(0)} / \gamma_{12}^{(0)}$. Enforcing the above scheme results in the following dimensionless governing equations for the i th fluid:

$$\nabla^2 T_i = 0, \quad (5a)$$

$$\nabla^2 \mathbf{u}_i = \nabla p_i, \quad \nabla \cdot \mathbf{u}_i = 0. \quad (5b)$$

The dimensionless boundary conditions on the interface S_{ij} take the following form:

$$T_i = T_j, \quad \text{and} \quad \kappa_i \nabla T_i \cdot \hat{\mathbf{n}}_{ij} = \kappa_j \nabla T_j \cdot \hat{\mathbf{n}}_{ij}, \quad (6a)$$

$$\mathbf{u}_i \cdot (\mathbf{I} - \hat{\mathbf{n}}_{ij} \hat{\mathbf{n}}_{ij}) = \mathbf{u}_j \cdot (\mathbf{I} - \hat{\mathbf{n}}_{ij} \hat{\mathbf{n}}_{ij}), \quad (6b)$$

$$\mathbf{u}_i \cdot \hat{\mathbf{n}}_{ij} = \mathbf{u}_j \cdot \hat{\mathbf{n}}_{ij} = (\mathbf{U}_3 - \mathbf{U}_2) \cdot \hat{\mathbf{n}}_{23} \delta_{i2} \delta_{j3}, \quad (6c)$$

$$[\lambda_i \boldsymbol{\tau}_i - \lambda_j \boldsymbol{\tau}_j] \cdot \hat{\mathbf{n}}_{ij} = \frac{1}{\text{Ca}} [\gamma_{ij} (\nabla \cdot \hat{\mathbf{n}}_{ij}) \hat{\mathbf{n}}_{ij} - \nabla_s^{(ij)} \gamma_{ij}]. \quad (6d)$$

The dimensionless far-field conditions become $\mathbf{u}_1 = [1 - (r^2 \sin^2 \theta / R^2) - U_2] \hat{\mathbf{e}}_z$ and $T_1 \sim z$ as $|\mathbf{r}| \rightarrow \infty$, and finally the boundedness condition in the inner drop reads $|\mathbf{u}_3| < \infty$ and $|p_3| < \infty$, when $r < R_l$. In Eq. (6d), Ca is the capillary number, defined as [61] $\text{Ca} = \mu_1 U_c / \gamma_{12}^{(0)}$. The dimensionless surface tension on the interface S_{ij} may be written as follows:

$$\gamma_{12} = 1 - \text{Ca Ma } T_{12} \quad \text{and} \quad \gamma_{23} = \gamma - \beta \text{ Ca Ma } T_{23}. \quad (7)$$

In Eq. (7), the Marangoni number, defined as [30,32,61] $\text{Ma} = \beta_{12} G' R'_O / \mu_1 U_c$, dictates the ratio of the induced Marangoni stresses to the viscous stresses [61]. We later show that Ma plays a key role in altering the drop velocities in the presence of an imposed temperature gradient.

B. Asymptotic analysis for approximately spherical drops

In the limit of low capillary number [$\text{Ca} \ll O(1)$], the drops remain nearly spherical, experiencing very little deformation. This allows us to expand any variable Ξ (such as \mathbf{u} and p) in a regular asymptotic series in Ca, as follows [34]:

$$\Xi = \Xi^{(0)} + \text{Ca } \Xi^{(1)} + O(\text{Ca}^2). \quad (8)$$

Now, for the special case of concentric drops, the equations for the interface S_{ij} , in terms of Ca, may be written using the spherical coordinates as follows [34]: $F_{12} = r - [1 + \text{Ca } f_{12}^{(\text{conc})}(\theta) + \dots]$ and $F_{23} = r - [R_l + \text{Ca } f_{23}^{(\text{conc})}(\theta) + \dots]$. The unit outward normals to these interfaces therefore become [up to $O(\text{Ca})$] $\hat{\mathbf{n}}_{ij} = \hat{\mathbf{e}}_r - \text{Ca } \nabla_s f_{ij}^{(\text{conc})}(\theta)$. In the case of eccentric configurations as shown in Fig. 2, a bispherical coordinate system (ξ, η, φ) [58] is required to simultaneously define the surfaces of both the drops. In this case, the equations for surfaces S_{ij} are defined as follows [34]: $F_{12} = \xi - [\pm \xi_1 + \text{Ca } f_{12}(\eta) + \dots]$ and $F_{23} = \xi - [\pm \xi_2 + \text{Ca } f_{23}(\eta) + \dots]$, where ξ_i is the location of the i th interface; see Sec. IV for more details. The surface normal at interface S_{ij} in this coordinate

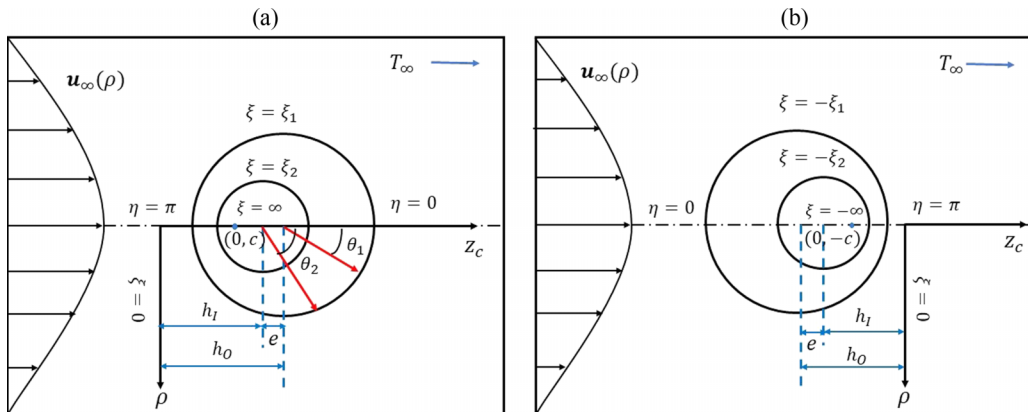


FIG. 2. Schematic representation of the bispherical coordinates (ξ, η, φ) to describe an eccentric compound drop. There are two possible configurations: (a) the “upstream configuration” ($\xi > 0$) and (b) the “downstream configuration” ($\xi < 0$). The outer and the inner drop surfaces are located at $\pm\xi_1$ and $\pm\xi_2$, respectively. The reference cylindrical coordinates (ρ, φ, z_c) , as discussed in Sec. II (see Fig. 1), have also been shown.

system has the following form: $\hat{\mathbf{n}}_{ij} = \hat{\mathbf{i}}_\xi - \text{Ca} \nabla_s f_{ij}(\eta)$. In the above expressions for the shape of the interface, f_{ij} denotes the $O(\text{Ca})$ deviation from a spherical surface.

In what follows, we shall only consider the leading-order terms (i.e., $\Xi^{(0)}$'s) for the flow variables (\mathbf{u}, p, T , etc.) and determine the $O(\text{Ca})$ deformation from there. We shall *a posteriori* verify that the deviation from the basic spherical shape remains quite small, even when Ca is relatively large (e.g., $\text{Ca} \sim 0.2$), which enables us to justify considering only the leading-order terms in our analysis. We reiterate that one of the focal points of the analysis will be to investigate, in detail, the effect of eccentricity on the leading-order dynamics and deformation of the drops in the given circumstances; so far, this has not been extensively addressed in the literature. From now on, unless otherwise mentioned, the “(0)” superscript from all the leading-order variables will be dropped for ease of representation and any variable such as $\mathbf{u}, \hat{\mathbf{n}}_{ij}$, etc., will indicate leading-order terms in the expansion (8). Finally, we note that although our analysis will mainly revolve around eccentric drops, it is possible to write closed-form analytical solutions for the relevant quantities (such as $\mathbf{u}, p, f_{ij}^{(\text{conc})}$, etc.) in the special case of concentric compound drops using spherical coordinates, as discussed in Sec. II. A brief summary of this special case has been included in Sec. S1 of the Supplemental Material [62].

IV. ANALYSIS FOR ECCENTRIC COMPOUND DROPS

A. The basic geometry

There are two possible eccentric configurations, as shown in Fig. 2. Panel (a) depicts the “upstream configuration,” where the inner drop’s center of mass lies behind the outer drop center ($\Delta z < 0$). Panel (b) shows the “downstream configuration,” where the inner drop’s center of mass lies ahead of the outer drop center ($\Delta z > 0$). Depending on the configuration, the origin of the bispherical coordinate system is either located behind or ahead of the outer drop. The interfaces of outer and inner drops are expressed in bispherical coordinates as $\xi = \pm\xi_1$ and $\xi = \pm\xi_2$, respectively, for upstream ($\xi > 0$) and downstream ($\xi < 0$) configurations. In Fig. 2(a), θ_1 and θ_2 , respectively, represent the polar angles of points lying on the outer and inner drops, measured from the positive z axis. The bispherical and cylindrical coordinates are related as follows [57,58]:

$$\rho = \frac{c \sqrt{1 - \zeta^2}}{\cosh \xi - \zeta}, \quad z_c = \frac{c \sinh \xi}{\cosh \xi - \zeta}, \quad \varphi = \varphi. \quad (9)$$

In Eq. (9), $\zeta = \cos \eta$ and c is a positive constant defined as [58] $c = \sinh |\xi_1| = R_I \sinh |\xi_2|$. In Fig. 2, the distances of the drop centers from the origin may be written as [58] $h_O = \pm \cosh \xi_1$ and $h_I = \pm R_I \cosh \xi_2$ for upstream (+) and downstream (-) configurations. The eccentricity is defined as the distance between the two drop centers and may be written as $e = |\Delta z| = |h_I - h_O|$. The coordinates of the drop interfaces may be chosen once the inner drop radius and the eccentricity are known, by using the following relation [34]:

$$\xi_1 = \cosh^{-1} \left(\frac{1 + e^2 - R_I^2}{2e} \right), \quad \xi_2 = \cosh^{-1} \left(\frac{1 - e^2 - R_I^2}{2eR_I} \right). \quad (10)$$

As the two drops move with different velocities in general, the eccentricity [$e(t)$] will evolve with time, as discussed later in Sec. IV D 2. Therefore, because of the quasisteady nature of the flow, the entire bispherical coordinate system changes with time and the description given above applies only to the configuration at a given time instant. As a result, the flow variables computed using the coordinates described in Eq. (10) will have an implicit time dependence because $e(t)$ and thereby ξ_1 and ξ_2 depend on time. It is important to note in this context that the initial value of eccentricity [$e(t=0)$] is expected to strongly depend on the particular generating mechanism to form the drops. However, as we show subsequently, our analysis remains valid for almost any value of initial eccentricity, provided the other assumptions, as stated in Sec. II, are satisfied; also see Sec. IV D 2 for further details.

B. Evaluation of the temperature field

The temperature in each phase evolves without any explicit dependence on the flow field and is governed by Eq. (5a), subject to (6a). Following the analysis by Sadhal [63], the problem of finding the temperature field may be reformulated by defining a scalar function χ , related to the heat flux as follows (for the i th fluid):

$$\mathbf{q}_i = -\kappa_i \nabla T_i = \kappa_i \nabla \times \left(\frac{\chi_i}{\rho} \hat{\mathbf{i}}_\phi \right). \quad (11)$$

As a result, the governing equation for temperature [see Eq. (5a)] is trivially satisfied. In bispherical coordinates, the gradient operator (∇) takes the form [58] $\nabla = \hat{\mathbf{i}}_\eta h_1 \partial/\partial\eta + \hat{\mathbf{i}}_\xi h_2 \partial/\partial\xi + \hat{\mathbf{i}}_\phi h_3 \partial/\partial\phi$, where h_1, h_2, h_3 are the metric coefficients, given by [58] $h_1 = h_2 = (\cosh \xi - \zeta)/c$ and $h_3 = (\cosh \xi - \zeta)/(c\sqrt{1 - \zeta^2})$. The governing equation for χ may be deduced by noting that $\nabla \times \mathbf{q}_i = 0$, which yields $\nabla \times \nabla \times (\chi_i/\rho) \hat{\mathbf{i}}_\phi = 0$. This may be further simplified to $\mathcal{E}^2 \chi_i = 0$, where \mathcal{E}^2 in bispherical coordinates is given by [64]

$$\mathcal{E}^2 \equiv \frac{(\cosh \xi - \zeta)}{c^2} \left[\frac{\partial}{\partial \xi} \left\{ (\cosh \xi - \zeta) \frac{\partial}{\partial \xi} \right\} + (1 - \zeta^2) \frac{\partial}{\partial \zeta} \left\{ (\cosh \xi - \zeta) \frac{\partial}{\partial \zeta} \right\} \right]. \quad (12)$$

The general solution for χ may be expressed as [65]

$$\chi = (\cosh \xi - \zeta)^{-\frac{1}{2}} \sum_{n=0}^{\infty} \left[a_n \cosh \left(n + \frac{1}{2} \right) \xi + b_n \sinh \left(n + \frac{1}{2} \right) \xi \right] C_{n+1}^{-\frac{1}{2}}(\zeta), \quad (13)$$

where $C_n^{-\frac{1}{2}}(x)$ is the Gegenbauer polynomial of degree $-1/2$ and order n . It may be verified that the leading-order far-field condition for temperature becomes [52] $\chi_1 \rightarrow \rho^2/2$, as $\xi, \eta \rightarrow 0$, while the boundedness condition simply indicates $|\chi_3| < \infty$, when $\xi \rightarrow \pm\infty$. Considering these conditions,

the following forms of χ_i are chosen for the i th fluid [52]:

$$\chi_1 = \frac{\rho^2}{2} + (\cosh \xi - \zeta)^{-\frac{1}{2}} \sum_{n=0}^{\infty} a_n \sinh \left(n + \frac{1}{2} \right) \xi C_{n+1}^{-\frac{1}{2}}(\zeta), \quad (14a)$$

$$\chi_2 = (\cosh \xi - \zeta)^{-\frac{1}{2}} \sum_{n=0}^{\infty} \left(c_n e^{(n+\frac{1}{2})(\xi-\xi_2)} + d_n e^{-(n+\frac{1}{2})(\xi-\xi_2)} \right) C_{n+1}^{-\frac{1}{2}}(\zeta), \quad (14b)$$

$$\chi_3 = (\cosh \xi - \zeta)^{-\frac{1}{2}} \sum_{n=0}^{\infty} e_n e^{\mp(n+\frac{1}{2})(\xi-\xi_2)} C_{n+1}^{-\frac{1}{2}}(\zeta). \quad (14c)$$

In Eq. (14c), wherever the \pm or the \mp sign appears, it is implied that the upper sign (i.e., $+$ when \pm appears) applies to the upstream configuration and the lower sign (i.e., $-$ when \pm appears) applies to the downstream configuration. This same convention has also been followed for the rest of the paper, unless otherwise mentioned. The required boundary conditions for χ on the drop interfaces may be derived from (6a); on the interface S_{ij} (at $\xi = \pm\xi_1$ or $\pm\xi_2$), they take the following form [52]: $\partial\chi_i/\partial\xi = \partial\chi_j/\partial\xi$ and $\kappa_i\chi_i = \kappa_j\chi_j$. These conditions can be transformed into a linear system of algebraic equations for the coefficients, by using recurrence relations and orthogonality property of the Gegenbauer polynomials, along with a few well-known identities, as described in Appendix A 1. The resulting algebraic equations have to be solved numerically to determine the four unknown coefficients (a_n, c_n, d_n, e_n for each n) in Eqs. (14). These equations have been included in Appendix A 2 a. It is observed that the $(n-1)$ th, n th, and the $(n+1)$ th modes in the aforesaid equations are coupled and hence this system of equations has to be truncated after a certain number of terms (say, N), in order to compute the solutions. It is further noted that the suitable choice of N for accurate solutions strongly depends on the eccentricity [52]. Further details on the values of N have been included in Appendix A 2 a. This completes the solution for the temperature field. For the purpose of future calculations, it is important to note how temperature gradients are related to χ and its derivatives; these relations may be summarized as

$$q_\xi^{(i)} = -\kappa_i \frac{(\cosh \xi - \cos \eta)}{c} \frac{\partial T_i}{\partial \xi} = \kappa_i \frac{(\cosh \xi - \cos \eta)^2}{c^2 \sin \eta} \frac{\partial \chi_i}{\partial \eta}, \quad (15a)$$

$$q_\eta^{(i)} = -\kappa_i \frac{(\cosh \xi - \cos \eta)}{c} \frac{\partial T_i}{\partial \eta} = -\kappa_i \frac{(\cosh \xi - \cos \eta)^2}{c^2 \sin \eta} \frac{\partial \chi_i}{\partial \xi}. \quad (15b)$$

C. Evaluation of the flow field

The leading-order governing equations for the flow are given by (5b). Because of the axisymmetric nature of the flow, we can make use of the Stokes stream function (Ψ), which allows us to write the equations of motion for the i th fluid in the form [58] $\mathcal{E}^4\Psi_i = 0$. The general solution for Ψ , in bispherical coordinates, may be expressed for the i th fluid as [64]

$$\Psi_i = (\cosh \xi - \zeta)^{-3/2} \sum_{n=0}^{\infty} W_n^{(i)}(\xi) C_{n+1}^{-\frac{1}{2}}(\zeta). \quad (16)$$

In Eq. (16), $W_n^{(i)}$ has the following form [34]: $W_n^{(i)} = A_n^{(i)} e^{(n-\frac{1}{2})\xi} + B_n^{(i)} e^{(n+\frac{3}{2})\xi} + C_n^{(i)} e^{-(n-\frac{1}{2})\xi} + D_n^{(i)} e^{-(n+\frac{3}{2})\xi}$. The velocity components (u_ξ and u_η) in the bispherical coordinates are related to the stream function Ψ as follows [34]:

$$u_\xi^{(i)} = \frac{(\cosh \xi - \zeta)^2}{c^2 \sin \eta} \frac{\partial \Psi_i}{\partial \eta} \quad \text{and} \quad u_\eta^{(i)} = -\frac{(\cosh \xi - \zeta)^2}{c^2 \sin \eta} \frac{\partial \Psi_i}{\partial \xi}. \quad (17)$$

Using Eq. (17), the far-field condition in the outermost fluid (phase 1) may now be recast as $\Psi_1 = -(1 - U_2)\rho^2/2 + \rho^4/4R^2$, as $\xi \rightarrow 0$. Using Eq. (9), along with some well-known identities (see

Appendix A 1), it may be shown that when $\xi \rightarrow 0$, Ψ_1 may be written in the following form [34]:

$$\Psi_1 = (\cosh \xi - \zeta)^{-3/2} \sum_{n=0}^{\infty} (\tilde{c}_n e^{\mp(n-\frac{1}{2})\xi} + \tilde{d}_n e^{\mp(n+\frac{3}{2})\xi}) C_{n+1}^{-\frac{1}{2}}(\zeta), \quad (18)$$

where the constants \tilde{c}_n and \tilde{d}_n have the following expressions [34]:

$$\tilde{c}_n = -\frac{n(n+1)c^2}{\sqrt{2}(2n-1)} \left[(1-U_2) + \frac{2c^2}{3R^2}(n-1)(n-2) \right], \quad (19a)$$

$$\tilde{d}_n = \frac{n(n+1)c^2}{\sqrt{2}(2n+3)} \left[(1-U_2) + \frac{2c^2}{3R^2}(n+2)(n+3) \right]. \quad (19b)$$

The boundedness condition in the inner core becomes $|\Psi_3| < \infty$, as $\xi \rightarrow \pm\infty$. In view of this and the far-field conditions, as expressed in Eq. (18), we may choose appropriate forms for $W_n^{(i)}$ for the i th phase ($i = 1, 2, 3$) as follows [34]:

$$W_n^{(1)} = A_n e^{\pm(n-\frac{1}{2})\xi} + B_n e^{\pm(n+\frac{3}{2})\xi} + \tilde{c}_n e^{\mp(n-\frac{1}{2})\xi} + \tilde{d}_n e^{\mp(n+\frac{3}{2})\xi}, \quad (20a)$$

$$W_n^{(2)} = E_n e^{\pm(n-\frac{1}{2})\xi} + F_n e^{\pm(n+\frac{3}{2})\xi} + G_n e^{\mp(n-\frac{1}{2})\xi} + H_n e^{\mp(n+\frac{3}{2})\xi}, \quad (20b)$$

$$W_n^{(3)} = \hat{C}_n e^{\mp(n-\frac{1}{2})\xi} + \hat{D}_n e^{\mp(n+\frac{3}{2})\xi}. \quad (20c)$$

The stream function in (16) with the $W_n^{(i)}$'s given in Eqs. (20) may be completely determined using the boundary conditions on the two interfaces, as mentioned in (6b)–(6d). On the outer drop surface (i.e., $\xi = \pm\xi_1$), these conditions become [34] $u_\eta^{(1)} = u_\eta^{(2)}$; $u_\xi^{(1)} = u_\xi^{(2)} = 0$; and $\tau_{\xi\eta}^{(1)} - \lambda_2 \tau_{\xi\eta}^{(2)} = \mp \text{Ma} h_1 \partial T_1 / \partial \eta$. On the inner drop surface ($\xi = \pm\xi_2$), the boundary conditions take the form $u_\eta^{(2)} = u_\eta^{(3)}$; $u_\xi^{(2)} = u_\xi^{(3)} = (\mathbf{U}_3 - \mathbf{U}_2) \cdot \hat{\mathbf{i}}_\xi$; and $\lambda_2 \tau_{\xi\eta}^{(2)} - \lambda_3 \tau_{\xi\eta}^{(3)} = \mp \beta \text{Ma} h_1 \partial T_3 / \partial \eta$.

The boundary conditions mentioned above essentially stem from the continuity of tangential velocity, the kinematic condition, and tangential stress balance, respectively. The tangential stress balance condition at the interface S_{ij} uses Eq. (7) and also involves the surface gradient operator, which in bispherical coordinates reads $\nabla_s = \hat{\mathbf{i}}_\eta h_1 \partial / \partial \eta + \hat{\mathbf{i}}_\phi h_3 \partial / \partial \phi$. Implementation of the boundary conditions also requires knowledge of the shear stress component $\tau_{\xi\eta}$, which in the i th fluid can be expressed as [66] $\tau_{\xi\eta}^{(i)} = h_2 [\partial u_\eta^{(i)} / \partial \xi - h_1 u_\xi^{(i)} \partial(1/h_2) / \partial \eta] + h_1 [\partial u_\xi^{(i)} / \partial \eta - h_2 u_\eta^{(i)} \partial(1/h_1) / \partial \xi]$. This expression can be further simplified by using Eqs. (16), (17), along with the identities mentioned in Appendix A 1, and the simplified form has been included in Appendix A 2 b; see Eq. (A7) therein.

The eight unknown coefficients, $A_n, B_n, E_n, F_n, G_n, H_n, \hat{C}_n$, and \hat{D}_n in Eqs. (20), may be computed from the eight boundary conditions (four conditions on each interface) mentioned above. To this end, expressions for the velocity and stress components as given in Eqs. (17)–(20), (A7), and $\partial T_{ij} / \partial \eta$ from Eq. (15b), along with the orthogonality properties of the Gegenbauer polynomials, may be used to deduce a system of eight linear algebraic equations for each mode n . These equations have been included in Appendix A 2 c and have to be solved numerically to compute the unknown coefficients.

D. Evaluation of instantaneous droplet velocities and the eccentricity

1. The droplet velocity estimations

As mentioned earlier, the drop velocities (U_2 and U_3) are not known *a priori* and hence have to be computed as part of the solution. This may be done by simply equating the net force on each of the drops to zero [34]. To this end, it is helpful to note that the coefficients A_n, B_n, E_n, \dots , etc., linearly depend on U_2 and U_3 . For instance, one may write $A_n = \mathcal{Y}_1^{(1)}(\mathbf{\Lambda}, e(t); n) + \mathcal{Y}_2^{(1)}(\mathbf{\Lambda}, e(t); n)U_2 + \mathcal{Y}_3^{(1)}(\mathbf{\Lambda}, e(t); n)U_3$, where $\mathbf{\Lambda} = [\lambda_2, \lambda_3, \text{Ma}, R_1, \kappa_2, \kappa_3, R]$ is the parameter matrix, which also includes fluid properties. Other coefficients may also be written in similar forms (see

Appendix A 2 c). Noting that the characteristic force is $F_c = \mu_i U_c R'_O$, the net force (dimensionless) acting on each drop may be expressed as [12,34,57]

$$F_{\text{outer}} = \frac{4\sqrt{2}\pi}{c} \sum_{n=0}^{\infty} (A_n + B_n) = 0, \quad F_{\text{inner}} = \frac{4\sqrt{2}\pi}{c} \sum_{n=0}^{\infty} (E_n + F_n) = 0. \quad (21)$$

Upon inserting the linear relations between the coefficients A_n, B_n, E_n, \dots and U_2 and U_3 , Eq. (21) would yield a pair of independent linear algebraic equations for the two variables U_2 and U_3 , which may be solved to determine the drop velocities.

2. Evolution of the eccentricity

It may be shown [34] (as we discuss in Sec. V) that the two drops generally do not move with the same velocity in a Poiseuille flow, which implies that the eccentricity (distance between the drop centers) slowly changes with time, leading to an implicit time dependence of the entire flow field. This implicit unsteady nature of the flow is captured in both the interface coordinates (i.e., ξ_1 and ξ_2), as well as the drop velocities (U_2 and U_3), since all of them depend explicitly on $e(t)$ or, equivalently, on $\Delta z(t)$. The droplet positions with respect to each other vary as $\Delta z(t) = h_I(t) - h_O(t)$ (see Fig. 2). Differentiating on both sides, we get [34]

$$\frac{d\Delta z(t)}{dt} = U_3(\Delta z(t), \Lambda) - U_2(\Delta z(t), \Lambda). \quad (22)$$

From (22), the eccentricity may be determined by using the relation $e(t) = |\Delta z(t)|$. Equation (22) may be solved, subject to a given initial condition, representing an initial configuration, to determine how $|\Delta z(t)|$ and hence the eccentricity changes with time. Once $e(t)$ is known, the drop velocities may be determined using Eq. (21). Equation (22) is nonlinear in nature and this has strong implications on how the eccentricity evolves, as we show later. Because of slow temporal evolution (quasisteady assumption), this equation may be solved using an explicit time-marching scheme.

E. Evaluation of droplet deformation

The $O(\text{Ca})$ deformations (f_{12} and f_{23}) can be obtained from the leading-order normal stress balance equations, as mentioned in Eq. (6d). On the interface S_{ij} (i.e., $\xi = \pm\xi_1$ or $\pm\xi_2$), this condition may be expressed as [67]

$$\lambda_i p_i - \lambda_j p_j + \lambda_j \tau_{\xi\xi}^{(j)} - \lambda_i \tau_{\xi\xi}^{(i)} = \mp \frac{\gamma_{ij}}{\text{Ca}} (\mathbf{V} \cdot \hat{\mathbf{n}}_{ij}). \quad (23)$$

For the purpose of evaluating the normal stresses, it is important to note that the divergence of an axisymmetric vector \mathbf{V} , in bispherical coordinates, reads [58] $\nabla \cdot \mathbf{V} = h_1 h_2 h_3 [\partial(V_\eta)/(h_2 h_3)/\partial\eta + \partial(V_\xi/h_1 h_3)/\partial\xi]$. Therefore, taking divergence of surface normals and using the equations for surface tension (γ_{ij}) as given in (7), Eq. (23) for the outer drop interface S_{12} (i.e., $\xi = \pm\xi_1$) becomes [68]

$$\begin{aligned} & \pm \frac{1}{c} \left[(\cosh \xi - \zeta)^3 \frac{d}{d\zeta} \left\{ \frac{1 - \zeta^2}{(\cosh \xi - \zeta)^2} \frac{df_{12}}{d\zeta} \right\} + \frac{2}{\text{Ca}} \sinh \xi + 2f_{12} \cosh \xi - 2\text{Ma}T_{12} \sinh \xi \right] \\ & = \lambda_2 p_2 - p_1 + \tau_{\xi\xi}^{(1)} - \lambda_2 \tau_{\xi\xi}^{(2)}. \end{aligned} \quad (24)$$

Similarly, the normal stress balance on the inner drop surface S_{23} ($\xi = \pm\xi_2$) reads [68]

$$\begin{aligned} & \pm \frac{1}{c} \left[\gamma (\cosh \xi - \zeta)^3 \frac{d}{d\zeta} \left\{ \frac{1 - \zeta^2}{(\cosh \xi - \zeta)^2} \frac{df_{23}}{d\zeta} \right\} + \frac{2\gamma}{\text{Ca}} \sinh \xi + 2\gamma f_{23} \cosh \xi - 2\text{Ma}\beta T_{23} \sinh \xi \right] \\ & = \lambda_3 p_3 - \lambda_2 p_2 + \lambda_2 \tau_{\xi\xi}^{(2)} - \lambda_3 \tau_{\xi\xi}^{(3)}. \end{aligned} \quad (25)$$

An equation for the pressure in the i th fluid (p_i) may be derived in terms of the stream function Ψ_i , using the momentum equations (5b), as follows [67,68]:

$$\frac{\partial p_i}{\partial \xi} = -\frac{(\cosh \xi - \zeta)}{c} \frac{\partial(\mathcal{E}^2 \Psi_i)}{\partial \zeta}, \quad \frac{\partial p_i}{\partial \zeta} = \frac{(\cosh \xi - \zeta)}{c(1 - \zeta^2)} \frac{\partial(\mathcal{E}^2 \Psi_i)}{\partial \xi}. \quad (26)$$

Using Eq. (16) for Ψ_i , one may evaluate $\mathcal{E}^2 \Psi_i$ for the i th fluid [68], which has been included in Appendix A 3 a. Because of the imposed background flow, the pressure far away from the drop is not uniform, but rather will vary linearly with distance. Therefore, the total pressure may be written as the sum of a nonzero background pressure ($p^{(b)}$), present everywhere, and a disturbance ($p_i^{(d)}$) caused by the presence of the drop, as follows: $p_i = p^{(b)} + p_i^{(d)}$. Note that $dp^{(b)}/dz_c = -4/R^2$, from which $p^{(b)}$ may be expressed in bispherical coordinates using Eq. (9), along with the identities given in Appendix A 1, and takes the following form:

$$p^{(b)} = \mp \frac{\mathcal{F} \sqrt{(\cosh \xi - \zeta)}}{c^3} \sum_{n=0}^{\infty} (2n+1) e^{\mp(n+\frac{1}{2})\xi} P_n(\zeta) + \frac{4h_0}{R^2} + C_b. \quad (27)$$

In Eq. (27), $P_n(\zeta)$ is the Legendre polynomial of degree 1 and order n , C_b is a constant yet to be determined, and $\mathcal{F} = 4c^4 \sqrt{2}/R^2$. Now, the momentum equations (5b) dictate that the pressure is harmonic (i.e., $\nabla^2 p_i = 0$) [68]. Since the background pressure trivially satisfies the Laplace equation, it follows that the disturbance pressure ($p_i^{(d)}$) in the i th fluid will also satisfy $\nabla^2 p_i^{(d)} = 0$. The general solution for the disturbance pressure in the i th fluid is therefore given by [68]

$$p_i^{(d)} = \frac{\sqrt{(\cosh \xi - \zeta)}}{c^3} \sum_{n=0}^{\infty} [\alpha_n^{(i)} e^{\pm(n+\frac{1}{2})\xi} + \beta_n^{(i)} e^{\mp(n+\frac{1}{2})\xi}] P_n(\zeta) + \Pi_i. \quad (28)$$

In Eq. (28), the Π_i 's are constants, yet to be determined. One may further note from Eq. (28) that $\alpha_n^{(3)} = 0$, because p_3 has to be bounded in the inner drop. From Eqs. (27) and (28), the total pressure for the i th fluid ($i = 1, 2, 3$) can be written as

$$p_i = \frac{\sqrt{(\cosh \xi - \zeta)}}{c^3} \sum_{n=0}^{\infty} [\alpha_n^{(i)} e^{\pm(n+\frac{1}{2})\xi} + [\beta_n^{(i)} \mp (2n+1)\mathcal{F}] e^{\mp(n+\frac{1}{2})\xi}] P_n(\zeta) + \frac{4h_0}{R^2} + \Pi_i. \quad (29)$$

In Eq. (29), the constant C_b from Eq. (27) has been absorbed in Π_i . The coefficients $\alpha_n^{(i)}$, $\beta_n^{(i)}$, etc., may be uniquely determined using the condition that the disturbance pressure must vanish far away from the compound drop. The detailed expressions for these coefficients along with an outline of how to evaluate them have been included in Appendix A 3 b. The final piece of the puzzle in Eq. (23) is the normal viscous stress components in the i th fluid ($\tau_{\xi\xi}^{(i)}$, $i = 1, 2, 3$), which may be written as [58,67] $\tau_{\xi\xi}^{(i)} = 2h_2 [\partial u_{\xi}^{(i)}/\partial \xi + h_1 u_{\eta}^{(i)} \partial(1/h_2)/\partial \eta]$. Detailed expressions for the normal stresses have been included in Appendix A 3 c.

From Eqs. (24) and (25), we observe that the interfacial temperature (T_{ij}) is also required in the normal stress balance. The temperature on both the interfaces may be evaluated by numerically integrating $\partial T_{ij}/\partial \eta$ from Eqs. (15). However, to determine the temperature uniquely, we need to specify its value at least at one point in the domain, preferably lying on either of the drop surfaces. To this end, as discussed in Sec. II, we enforce that on the outer drop surface, at $z = 0$ (in the spherical coordinates attached to the drop center; this is same as $z_c = h_0$), i.e., at $\theta_1 = \pi/2$ and $\xi = \pm \xi_1$ (or $r = 1$), $T_1 = T_2 = T_{12} = 0$. Essentially, this means that the point on the interface which is on the same vertical line as the outer drop center has $T = 0$. This is sufficient to determine temperatures uniquely at all positions on both the interfaces by numerically integrating (15). Finally, substituting Eqs. (29) and (A16) in the normal stress balance Eqs. (24) and (25) and after a bit of tedious algebra

we deduce the following equations for the deformation (f_{ij}) on the interface S_{ij} ($\xi = \pm\xi_1$ or $\pm\xi_2$):

$$\frac{d^2 f_{ij}}{d\xi^2} + \frac{2(1 - \zeta \cosh \xi)}{(1 - \zeta^2)(\cosh \xi - \zeta)} \frac{df_{ij}}{d\xi} + \frac{2 \cosh \xi}{(1 - \zeta^2)(\cosh \xi - \zeta)} f_{ij} = \mathcal{G}_{ij}(\zeta) + \hat{\mathcal{G}}_{ij}(\zeta) \Pi_{ij}, \quad (30)$$

where the appropriate value of ξ has to be used, depending on the interface under consideration. In Eq. (30), $\Pi_{12} = \lambda_2 \Pi_2 - \Pi_1 \mp 2 \sinh \xi_1 / (c \text{Ca})$ and $\Pi_{23} = \lambda_3 \Pi_3 - \lambda_2 \Pi_2 \mp 2\gamma \sinh \xi_2 / (c \text{Ca})$ are unknown constants and have to be determined as part of the solution. Expressions for the quantities $\mathcal{G}_{ij}(\zeta)$ and $\hat{\mathcal{G}}_{ij}(\zeta)$ have been included in Appendix A 3 d. The ODE in Eq. (30) has the following linearly independent, complementary solutions [67,68]: $f_{ij}^{(c)} = (1 - \zeta \cosh \xi)$ and $\hat{f}_{ij}^{(c)} = \{\sinh^2 \xi / \cosh \xi + (1/2)(1 - \zeta \cosh \xi) \ln[(1 + \zeta)/(1 - \zeta)]\}$. The complete solution for the deformation on the ij th interface [$f_{12}(\zeta)$ and $f_{23}(\zeta)$] then reads

$$f_{12}(\zeta) = C_{12} f_{12}^{(c)}(\zeta) + \hat{C}_{12} \hat{f}_{12}^{(c)}(\zeta) + \mathcal{I}_{12}(\zeta) + \Pi_{12} \hat{\mathcal{I}}_{12}(\zeta), \quad (31)$$

$$f_{23}(\zeta) = C_{23} f_{23}^{(c)}(\zeta) + \hat{C}_{23} \hat{f}_{23}^{(c)}(\zeta) + \mathcal{I}_{23}(\zeta) + \Pi_{23} \hat{\mathcal{I}}_{23}(\zeta). \quad (32)$$

In Eqs. (31) and (32), C_{ij} , \hat{C}_{ij} are unknown constants and $\mathcal{I}_{ij}(\zeta)$, $\hat{\mathcal{I}}_{ij}(\zeta)$ are the particular integrals, given by [69]

$$\mathcal{I}_{ij}(\zeta) = -f_{ij}^{(c)}(\zeta) \int_{-1}^{\zeta} \frac{\mathcal{G}_{ij}(x) \hat{f}_{ij}^{(c)}(x)}{\mathcal{W}_{ij}(x)} dx + \hat{f}_{ij}^{(c)}(\zeta) \int_{-1}^{\zeta} \frac{\mathcal{G}_{ij}(x) f_{ij}^{(c)}(x)}{\mathcal{W}_{ij}(x)} dx, \quad (33a)$$

$$\hat{\mathcal{I}}_{ij}(\zeta) = -f_{ij}^{(c)}(\zeta) \int_{-1}^{\zeta} \frac{\hat{\mathcal{G}}_{ij}(x) \hat{f}_{ij}^{(c)}(x)}{\mathcal{W}_{ij}(x)} dx + \hat{f}_{ij}^{(c)}(\zeta) \int_{-1}^{\zeta} \frac{\hat{\mathcal{G}}_{ij}(x) f_{ij}^{(c)}(x)}{\mathcal{W}_{ij}(x)} dx. \quad (33b)$$

In Eqs. (33), $\mathcal{W}_{ij}(x) = (\cosh \xi - x^2)/(1 - x^2)$, is the Wronskian of $f_{ij}^{(c)}(\zeta)$ and $\hat{f}_{ij}^{(c)}(\zeta)$, evaluated on the interface S_{ij} . Based on physical considerations, we may assert that f_{ij} remains bounded at $\eta = 0$ and may be assigned the finite value, say $f_{ij}(\eta = 0) = \Phi_{ij}$, where Φ_{ij} is a constant. Now, in the solutions for the droplet deformation [see Eqs. (31) and (32)], there are four unknown constants, namely C_{ij} , \hat{C}_{ij} , Π_{ij} , and Φ_{ij} . These may be determined using the following four conditions [67], applicable on both the interfaces ($\xi = \pm\xi_1$ and $\pm\xi_2$): (i) $df_{ij}/d\eta$ shall remain bounded at $\eta = 0$ and π ; (ii) the volume of both the drops will be conserved, which yields [67,68] $\int_{-1}^1 \{f_{ij}(\zeta)/(\cosh \xi - \zeta)^3\} d\zeta = 0$; (iii) the center of mass of both the drops will be unchanged, leading to [67,68] $\int_{-1}^1 \{f_{ij}(\zeta)/(\cosh \xi - \zeta)^4\} d\zeta = 0$. This completes the evaluation of the interfacial deformations.

V. RESULTS AND DISCUSSION

The main aim of our analysis is to bring out the effects of the externally imposed temperature gradient on the dynamics and deformation of the drops and in particular characterize the influence of eccentricity on the aforesaid factors. The effect of the external temperature gradient is best summarized by the following factors: (i) the Marangoni number ($\text{Ma} = \beta_{12} G' R'_O / \mu_1 U_c$), which dictates the extent of Marangoni stresses; (ii) the thermal conductivity ratios, κ_2 and κ_3 (recall that $\kappa_i = k_i/k_1$), which dictate the temperature distribution in the three phases, and finally, (iii) the eccentricity of the configuration [$\Delta z(t)$ or $e(t)$], which alters the temperature and the flow field, by changing the geometry. Therefore, in this section, we shall explore how the three indicators mentioned above influence the dynamics and deformation of the compound drop system.

At this stage, it is important to explore the probable range of values of various parameters, which play key roles in the present analysis. To this end, we consider the example of an oil-in-water-in-oil (O-W-O) double emulsion, with castor oil as the suspending medium as well as the inner core (fluids 1 and 3). We note the following properties of castor oil [70]: viscosity, $\mu_1 \sim 0.853 \text{ Pa s}$; thermal conductivity, $k_1 \sim 4.73 \text{ W m}^{-1} \text{ K}^{-1}$; thermal diffusivity, $\alpha_1 \sim O(10^{-5}) \text{ m}^2 \text{ s}^{-1}$; and the

surface tension of a castor oil–water interface is [71] $\gamma_{12}^{(0)} \sim 0.012 \text{ N m}^{-1}$. Then, for droplet sizes to the tune of $R'_o \sim 10^{-3} \text{ m}$ and characteristic velocity in the range [72,73] $U_c \sim O(10^{-5}) - O(10^{-3}) \text{ m/s}$, we deduce that the capillary number of the system lies in the range $\text{Ca} \sim O(10^{-3})$ to $O(10^{-1})$, which justifies the asymptotic expansion in Ca , on account of small deformation. On the other hand, owing to a lack of extensive studies on the measurement of β_{12} for castor oil–water interface, we may refer to some of the other existing studies on water [74] and assume $\beta_{12} \sim O(10^{-4})$ to $O(10^{-3}) \text{ N/m K}$. Then, for $G' \sim 50 \text{ K/m}$, one may deduce that $\text{Ma} \sim O(10^{-3})$ to $O(1)$. Similar ranges of Ma values have also been used previously in the literature [21,23]. At the same time, the above set of properties yields $\text{Re} \sim O(10^{-5})$ to $O(10^{-3})$ and $\text{Pe} \sim O(10^{-3})$ to $O(10^{-1})$, as mentioned earlier in Sec. II.

The rest of this section is arranged as follows. First, in Sec. VA, we validate our analysis by comparing its predictions with some of the earlier studies in the literature, as well as with other known results. This is followed by Sec. VB, where we probe into the variations in the droplet velocities as a function of the above indicators. In Sec. VC, a stability analysis (not the classical normal mode analysis though) of the inner drop is performed, in continuation with the preceding section. Finally, in Sec. VD, we shed light on how the drops deform and how the various factors control this. For the rest of the paper, we have chosen the surface tension ratio as [75] $\gamma = 1$ and $\beta = 1$.

A. Validation

We validate our semianalytical solutions in two separate ways. First, it is possible to write closed-form exact solutions for the droplet velocities and the deformation in the leading-order of Ca , when the drops are in concentric configuration. These solutions have been included in Sec. S1 of the Supplemental Material [62]. Therefore, the results for the small eccentricity limit ($e \ll 1$) may be directly compared with those of concentric compound drops, to assess the former's accuracy. The outer and inner droplet velocities (U_2 and U_3) for a concentric configuration are given in Eqs. (S2) and (S3) of the Supplemental Material [62], while the corresponding deformations may be obtained from Eq. (S6) therein. These closed-form solutions may in turn be compared in appropriate limiting cases to the work of Mandal *et al.* [34] and Borhan *et al.* [38]. These comparisons have been included in Sec. S1 of the Supplemental Material [62].

Second, although thermocapillary effects on eccentric compound drops in Poiseuille flows have not been addressed before, several studies on the migration of single drops [23,30,43,49,76] in the presence of imposed temperature gradients have been carried out. The single-drop limit in our analysis may be realized by enforcing $R_I \ll 1$ and those results will be compared with the work of Das *et al.* [30], who analyzed the motion of a single surfactant-laden droplet in nonisothermal Poiseuille flow, in the limit of weak interfacial convection ($\text{Pe}_s \ll 1$), and reported that the leading-order droplet velocity is independent of the surfactants. We shall further compare the deformation in the single-drop limit ($R_I \ll 1$) with the results of Hetsroni and Haber [60], who analyzed the motion of a drop suspended in a Poiseuille flow, at a distance b from the flow centerline. Their solutions for the deformation may be compared with ours by enforcing $b = 0$, and the two results match exactly as outlined in Eq. (S6) in Sec. S1 of the Supplemental Material [62].

Figures 3(a) and 3(b) show the comparison between the results obtained using an eccentric drop configuration with those of concentric drops, in the limit of small eccentricity ($e = 0.001$), for three different choices of the inner core radius, $R_I = 0.2, 0.4,$ and 0.8 , while values of other relevant parameters have been mentioned in the caption. Panels (a) and (b) showcase the outer and the inner drop velocities, respectively. We observe that the analysis using bispherical coordinates for low eccentricity match exactly with those of concentric drops, for all the cases reported in the figures. Further notice that here the imposed temperature gradients aid the movement of both the drops, as they speed up upon increasing Ma . However, the inner core size seems to influence the drop velocities in the opposite way. The inner drop velocity decreases with its size [see panel (b)], while at the same time, the outer drop velocity increases. Such variations may be best understood from Eqs. (S2) and (S3) of the Supplemental Material [62], which underline that the influence of R_I on

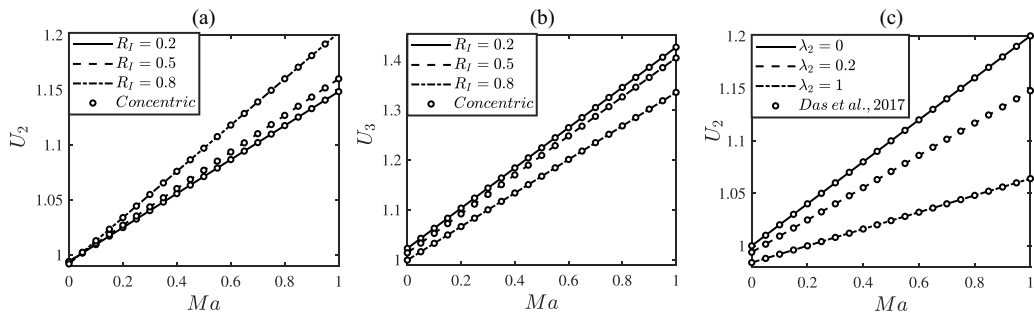


FIG. 3. (a) Comparison of outer drop velocity (U_2) vs Ma for eccentric drops (present study, denoted by lines) with $e = 0.001$ and concentric drops (circle), for different choices of inner drop size, $R_I = 0.2, 0.5,$ and 0.8 . (b) Comparison of inner drop velocity (U_3) vs Ma under the same scenario. Other relevant parameters in (a) and (b) are $R = 5, \lambda_2 = 0.2, \lambda_3 = 1, \kappa_2 = 3, \kappa_3 = 1$. (c) Comparison of U_2 vs Ma in the limit of single drop with $R_I = 0.001$ and $e = 0.001$, with the results of the work of Das *et al.* [30], for different choices of $\lambda_2 = 0, 0.2,$ and 1 , whereas $R = 5, \kappa_2 = 3$.

U_2 and U_3 strongly depends on the imposed temperature gradient as well as the coefficient \bar{B}_1 , and given the present set of parameters, increasing R_I increases the outer drop's velocity and decreases the inner drop's velocity.

Figure 3(c) compares the limiting case of a single drop ($R_I \ll 1$) as obtained from our analysis to those of Das *et al.* [30], for three choices of $\lambda_2 = 0, 0.2,$ and 1 . Note that the exact leading-order solutions in the limit of a single drop have been included in Eq. (S4) in Sec. S1 of the Supplemental Material [62]. When plotting the results from the analysis for eccentric drops, we have enforced $e = 0.001$, although this value is immaterial as long as R_I is sufficiently small. First note that the two sets of plots exhibit exact match. Second, as expected, the velocity of the drop decreases as its viscosity is increased.

A detailed account of the comparisons of droplet deformation for validation purposes has been included in Sec. S2 of the Supplemental Material [62].

B. Dynamics of the drops

In this section we investigate the effect of temperature field on the motion of eccentric compound drops in Poiseuille flow. We begin by analyzing the effect of Marangoni number (Ma) on the drops' velocities, computed from Eqs. (21). Notice that Ma can be finely tuned by varying the imposed temperature gradient G' , where $G' > 0$ indicates temperature increasing in the positive z direction and $G' < 0$ implies the opposite (see Fig. 1).

Figures 4(a) and 4(b) depict the variation in the normalized outer and inner droplet velocities $U_j/U_{j, Ma=0}$ for $j = 2, 3$ as a function of Ma , for different eccentricities: $e = 0.001, 0.1, 0.6, 0.78$, while other relevant parameters are mentioned in the caption. Noting that $U_{j, Ma=0}$ underlines the velocity in an isothermal flow, the ratio $U_j/U_{j, Ma=0}$ would thus shed light on the direct influence of thermocapillarity on the drop velocities. It is noted that in both upstream and downstream configurations, the same drop velocities are observed when eccentricity ($e = |\Delta z|$) is unaltered. The two panels clearly demonstrate that both the drops speed up when $Ma > 0$ (temperature increasing along z) and slow down when $Ma < 0$ (when temperature decreases along z), relative to isothermal flows. When $Ma > 0$, the temperature toward the rear end of the drops is smaller, which causes the surface tension in that part of the interface to be comparatively larger. This pulls the surrounding outer fluid (e.g., fluid 1 for interface S_{12}) toward the rear end of the interface and as a result the drop itself speeds up. Exactly opposite effect takes place when $Ma < 0$, slowing down the overall motion of the drops. The effect of eccentricity on the relative velocities is however more intriguing and depends on the direction of the applied temperature gradient. Notice that for $Ma < 0$,

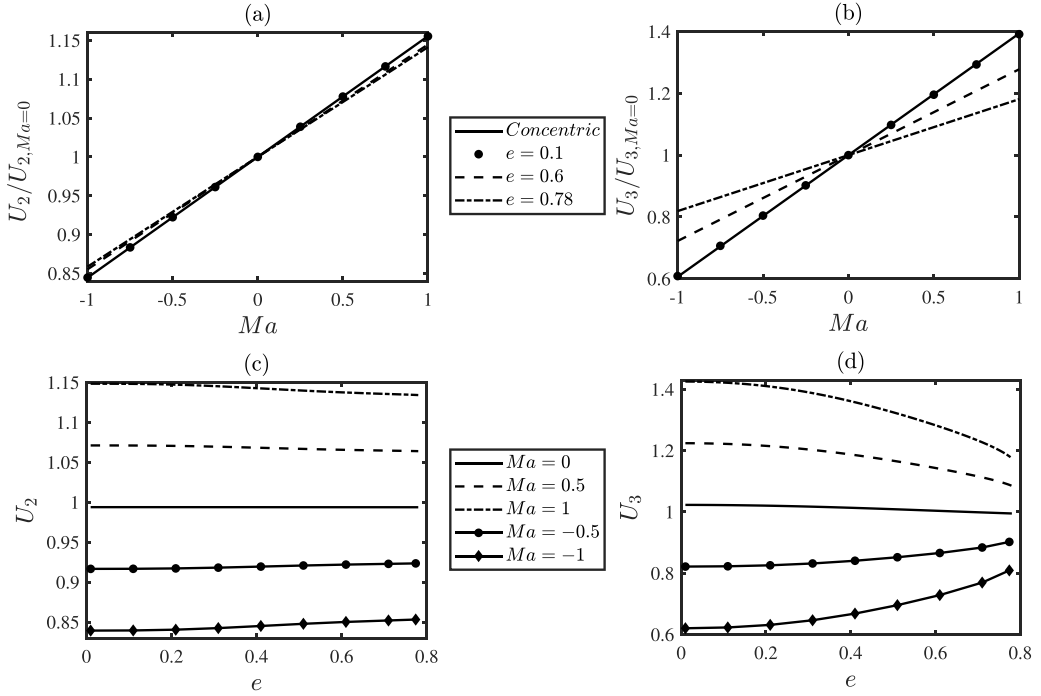


FIG. 4. Variation of normalized velocity (a) for outer drop ($U_2/U_{2, Ma=0}$) and (b) inner drop ($U_3/U_{3, Ma=0}$), as a function of Ma for different eccentricities $e = 0.78, 0.6, 0.1$, and 0.001 (concentric configuration). (c) Plot of U_2 vs e and (d) U_3 vs e , for various choices of $Ma = 0, \pm 0.5$, and ± 1 . Other relevant parameters are $R_I = 0.2$, $R = 5$, $\lambda_2 = 0.2$, $\lambda_3 = 1$, $\kappa_2 = 3$, $\kappa_3 = 1$.

a more eccentric configuration (i.e., larger e) results in an increase in drop velocities relative to an isothermal flow. The reverse is true when $Ma > 0$.

To understand the aforementioned variation in velocity with e , we may refer to Figs. 4(c) and 4(d), where the drop velocities [U_2 in panel (c) and U_3 in panel (d)] have been plotted as a function of e , for $Ma = 0$ (isothermal flow), ± 0.5 , and ± 1 , while values of other relevant parameters have been mentioned in the caption. Notice the twofold effect of eccentricity, when a temperature gradient is externally imposed. When $Ma = 0$ (isothermal flow), the drop velocities show very little variation with eccentricity, at least for the parameters chosen here. However, if the drops are exposed to positive temperature gradients, their velocities decrease with increasing eccentricity. On the other hand, when negative temperature gradients are imposed, their velocities increase with e . This underscores the profound effect an externally imposed temperature field can have on the drop velocities. The reason for such intriguing variation in the velocities may be attributed to how the interfacial tension varies in the presence of a temperature gradient. It may be shown (as we discuss in the next figure) that for $Ma > 0$, temperature gradients become smaller as the eccentricity increases. This means that the boost the drops receive from the resulting variations in surface tension also diminishes, which leads to a decrease in their velocities. The opposite happens when $Ma < 0$, which results in an increase in the drop velocities. Overall, we observe that both eccentricity and the temperature gradient (Ma) have more pronounced effects on the velocity of the inner core, which may vary by as much as 40%, even when $Ma \sim O(1)$.

The velocity variations shown in Fig. 4 may be better understood by looking into how the surface tension varies on the two surfaces, which in turn would also reflect the temperature variations along the interfaces. This has been shown in Fig. 5, where we plot γ_{12} vs θ_1 in panels (a) and (c) and γ_{23} vs θ_2 in panels (b) and (d), when the drops are in the upstream configuration (see Fig. 2).

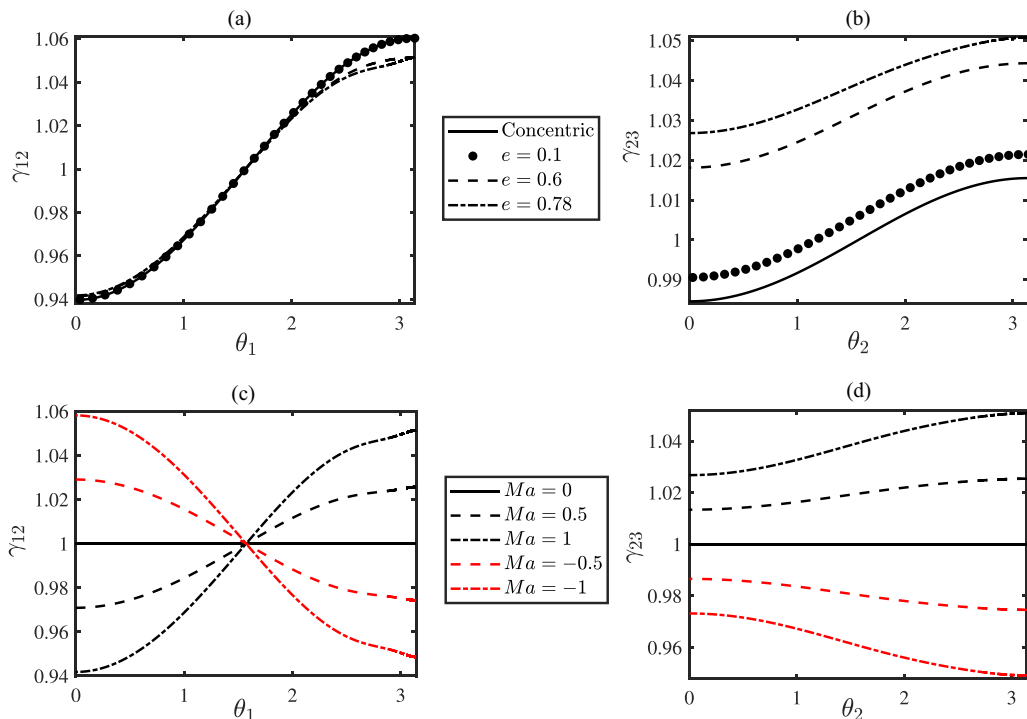


FIG. 5. Variations in γ_{ij} with θ_1 and θ_2 (as appropriate), for the upstream configuration: (a) across outer drop interface (γ_{12}) and (b) inner drop interface (γ_{23}), for different eccentricities, $e = 0$ (concentric configuration), 0.1, 0.6, and 0.78 and $Ma = 1$; (c) across outer drop interface (γ_{12}) and (d) inner drop interface (γ_{23}), for different $Ma = 0, \pm 0.5$, and ± 1 values with $e = 0.78$. Other relevant parameters are $R_l = 0.2$, $R = 5$, $\lambda_2 = 0.2$, $\lambda_3 = 1$, $\kappa_2 = 3$, $\kappa_3 = 1$, and $Ca = 0.1$.

In panels (a) and (b), variations in surface tension have been depicted for different eccentricities [$e = 0$ (concentric), 0.1, 0.6, and 0.78] when $Ma = 1$, while in panels (c) and (d), the effect of varying Ma at a fixed eccentricity ($e = 0.78$) has been illustrated. As expected, when $Ma > 0$, the surface tension decreases at both the interfaces, as we move from the rear of the drops ($\theta_1 = \theta_2 = \pi$) to its front ($\theta_1 = \theta_2 = 0$), which is the main cause behind the thermocapillary motion. The effect of eccentricity is far more pronounced for the inner core, as evident from panels (a) and (b), while for the outer drop the effect of e only becomes prominent at the rear end, close to $\theta_1 = \pi$. This is simply the effect of the inner drop, which in an upstream configuration with $e = 0.78$ resides very close to the outer interface (S_{12}), thus changing the temperature there. Notice from panel (b) that the overall surface tension at the inner interface (S_{23}) increases, as the configuration becomes strongly eccentric from being concentric. The reason may again be attributed to the upstream configuration, because of which the average temperature of the inner drop decreases as e increases, which ultimately leads to an increase in γ_{23} . Finally, panels (c) and (d) demonstrate the effect of imposed temperature gradient on the surface tension along the interface, wherein it may be observed that the nature of variation in γ_{ij} flips, when the direction of the external gradient is reversed, as indicated by $Ma < 0$. It is important to realize here that although the magnitudes of the gradients in γ_{ij} remain the same regardless of the configuration, absolute value of the surface tension changes, depending on whether the inner core is in the upstream or downstream configuration. As a result, it is expected that the drop velocities will not change, since they only depend on $|\Delta z| = e$, but the deformation of especially the inner drop will be different, as the configuration changes from upstream to downstream. We elaborate more on this in Sec. [VD](#).

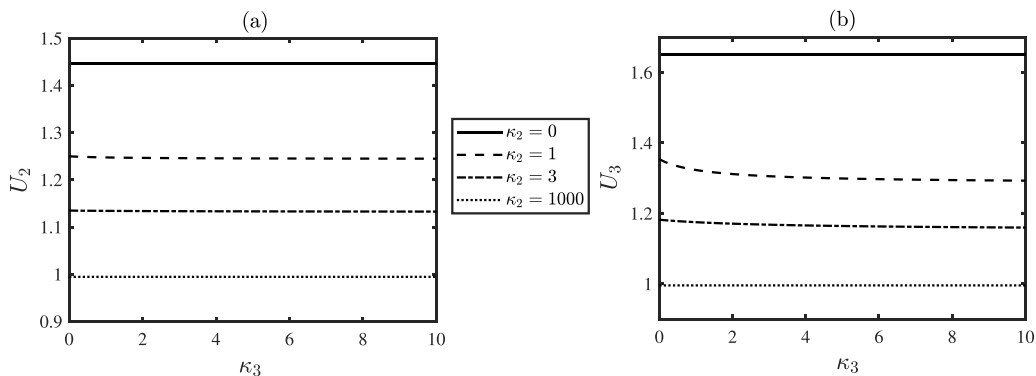


FIG. 6. Plot of U_2 vs κ_3 (inner drop's thermal conductivity) in panel (a) and of U_3 vs κ_3 in panel (b) for various κ_2 (outer drop conductivity) = 0, 1, 3, 1000. Other relevant parameters are $R_I = 0.2$, $R = 5$, $\lambda_2 = 0.2$, $\lambda_3 = 1$, $e = 0.78$, $\text{Ma} = 1$.

We have noted that the Marangoni stresses and hence the temperature field strongly influence the droplet velocities [through Eqs. (7)]. Noting that the interfacial temperatures are expected to be governed by the thermal conductivity ratios (κ_2 , κ_3), it is worth looking into their effects on the drop velocities. Figure 6 demonstrates the variations in the outer drop velocity (U_2) in panel (a) and the inner drop velocity U_3 in panel (b), as a function of κ_3 (thermal conductivity of the inner core), for different conductivity values of the outer drop, $\kappa_2 = 0, 1, 3, 1000$. It may be observed that both U_2 and U_3 are almost insensitive to κ_3 , albeit U_3 decreases slightly, as κ_3 increases. The temperature field is a weak function of κ_3 , which explains why the drop velocities are essentially independent of the inner core conductivity and hence the choice of κ_3 does not have a major influence on U_2 and U_3 . The outer drop's conductivity (κ_2), on the other hand, has a far stronger effect on the drop velocities. One expects that for larger κ_2 , the outer drop (fluid 2) is more thermally conducting, which will naturally diminish any temperature variations across the interface and hence will make the surface tension across the outer interface almost uniform. This will reduce the Marangoni stresses, which for $\text{Ma} > 0$ are responsible for speeding up the drops. Therefore, it is anticipated that the drop velocities should reduce with κ_2 , when $\text{Ma} > 0$. This is exactly what we observe in both the panels under consideration, wherein the slowest movement occurs for the largest κ_2 ($= 1000$) value.

C. Equilibrium and stability of the inner drop

It is evident from Figs. 3 and 4 that in a Poiseuille flow, in the absence of imposed temperature gradients (i.e., $\text{Ma} = 0$), the inner drop always moves faster than the outer drop, which leads to an ever increasing eccentricity and rules out the possibility of an equilibrium concentric configuration [35,36]. However, an external temperature gradient enables us to finely tune the drop velocities and especially influence the velocity of the inner drop. This poses two important questions: (i) Using an imposed temperature gradient, is it possible to achieve an equilibrium configuration in the compound drop, where both the drops move with the same velocity? (ii) If so, how "stable" would such an equilibrium be? These are the two questions we try to answer in this subsection. We reiterate that the "stability" here does not refer to a classical normal mode analysis.

The best way to investigate whether an equilibrium configuration (for any eccentricity) exists is to evaluate the relative velocity between the drops' center of masses: $U_2 - U_3$. This is what we do in Fig. 7(a), where the relative velocity as a function of Ma has been plotted for different eccentricities. An equilibrium configuration would imply $U_2 - U_3 = 0$; i.e., the drops will move with the same velocity. First, it is to be noted that for $\text{Ma} > 0$, $U_3 > U_2$ always and thus only $\text{Ma} < 0$ will be considered here. Notice that for small magnitudes of Ma , $U_2 - U_3 < 0$, for almost all values of e , indicating that the inner drop moves faster relative to the outer one, the difference being the

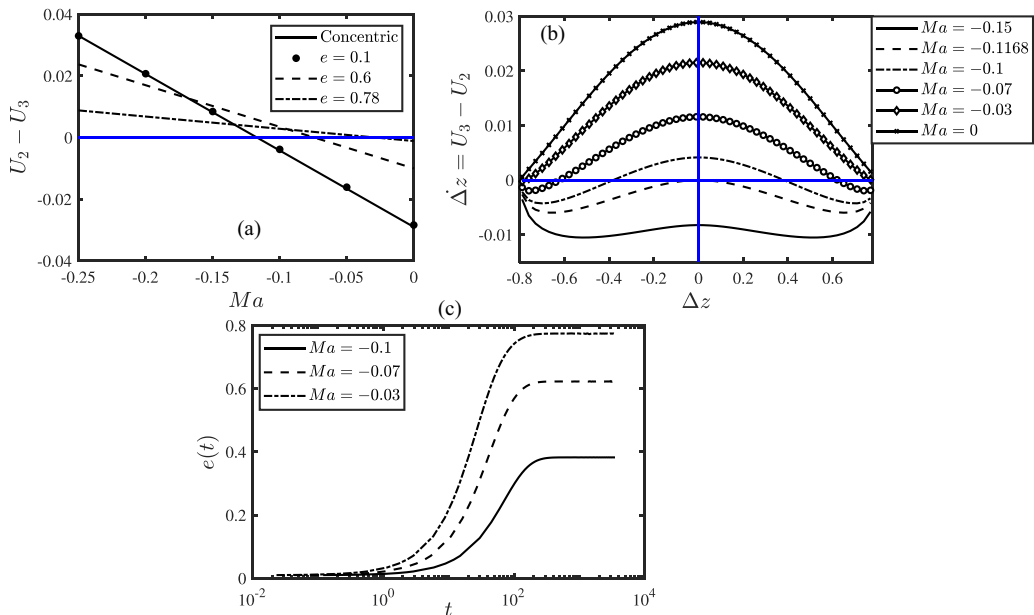


FIG. 7. (a) Variation in relative drop velocity ($U_2 - U_3$) with Ma for different eccentricities. (b) Phase plot of $\Delta \dot{z}$ vs Δz [from Eq. (22)] for different Ma values; see legend. (c) Evolution of eccentricity $e(t)$ with time (t), computed from Eq. (22), subject to the initial condition, $e(t = 0) = 0$, for various choices of $Ma = -0.1$, -0.07 , and -0.03 . Other relevant parameters are $R_I = 0.2$, $R = 5$, $\lambda_2 = 0.2$, $\lambda_3 = 1$, $\kappa_2 = 3$, and $\kappa_3 = 1$.

largest for a concentric configuration. However, as $|Ma|$ is increased (recall that $Ma < 0$ here, i.e., T decreases with z), we observe that $U_2 - U_3$ becomes positive, for all values of e (eccentricity). This shift in sign inevitably signals the existence of a certain Ma_* for each e , for which $U_2 = U_3$. It is further observed that this $|Ma_*|$ (the magnitude) required to achieve the equilibrium increases as the eccentricity decreases and hence the largest $|Ma_*|$ occurs for the concentric configuration, amounting to $Ma_* \approx -0.1168$. This also indicates that for $Ma < -0.1168$ and $Ma > 0$, there are no possible equilibrium configurations, while it is possible to have an equilibrium configuration at any eccentricity below a maximum limit, depending on the size of the inner core, by carefully choosing the imposed temperature gradient, such that $-0.1168 < Ma < 0$. We would like to emphasize that the above mentioned range of Ma , which may lead to a possible equilibrium, strongly depends on the size of the inner core. Notice that since $R_I = 0.2$ here, the maximum possible eccentricity the inner drop can achieve is $e = 0.8$. At this stage, it is important to realize that both U_2 and U_3 are the same irrespective of whether the drops are in downstream or upstream configurations, which is dictated by the sign of Δz . Since there are two possible choices of Δz (see Fig. 2) for each e , it follows from Fig. 7(a) that there will be one equilibrium position corresponding to each downstream and upstream configuration, having the same magnitude of Δz . Interestingly, the curve corresponding to $e = 0$ shows that an equilibrium concentric position is theoretically possible at a “critical” Marangoni number. This brings us to the second question posed at the beginning of this section, i.e., how to determine the stability of the equilibrium configurations arising herein.

The aforementioned stability may be assessed from a phase plot of Δz , based on Eq. (22), where the nature of the fixed points [59] can be insightful. The phase plot, i.e., $\Delta \dot{z}$ vs Δz for different Ma values (all negative), has been depicted in Fig. 7(b). There are several remarkable features to be noted from this figure. The equilibrium points corresponding to $U_2 - U_3 = 0$ would translate into fixed points on this graph [59], where $\Delta \dot{z} = 0$. Simply put, the equilibrium (or fixed) points are where the curves of $\Delta \dot{z}$ intersect the horizontal axis (Δz). First, note the symmetry in all the $\Delta \dot{z}$ curves, which prevails because the drop velocities do not depend on the sign of Δz . Second, we

observe that there are no fixed points when $Ma = -0.15$; this is in agreement with panel (a), which established that beyond $Ma = -0.1168$, an equilibrium configuration is not possible. Interestingly, when $Ma = Ma_c = -0.1168$, the $\Delta\dot{z}$ curve just touches the horizontal axis at $\Delta z = 0$. This signals the inception of the first possible equilibrium configuration, where the drops are concentric. The stability of this equilibrium point would depend on the slope $d(\Delta\dot{z})/d(\Delta z)$ evaluated at $\Delta z = 0$. If $d(\Delta\dot{z})/d(\Delta z) > 0$, the fixed point is unstable; otherwise if $d(\Delta\dot{z})/d(\Delta z) < 0$, the fixed point would be stable [59]. However, because of symmetry, it is obvious that $\{d(\Delta\dot{z})/d(\Delta z)\}_{\Delta z=0} = 0$ and hence the above arguments (which are based on linear analysis) do not directly apply. However, notice that $\Delta\dot{z} < 0 \forall \Delta z \neq 0$ when $Ma = Ma_c = -0.1168$, indicating that $\Delta\dot{z}$ does not change sign at $\Delta z = 0$ and hence the fixed point at $\Delta z = 0$ is unstable to disturbances toward $\Delta z < 0$. We may thus conclude that although it is theoretically possible to have an equilibrium concentric configuration for $Ma = Ma_c$, this will almost certainly be unstable and thus unachievable in practice.

Third, when $Ma > Ma_c$, there are always two fixed points (as discussed earlier), one for $\Delta z < 0$, corresponding to the upstream configuration, and another for $\Delta z > 0$, corresponding to the downstream configuration. Judging from the slope of the curves at these two fixed points, we immediately conclude that the downstream equilibrium configurations are stable and the upstream ones are unstable. Further note that it is possible to achieve a stable equilibrium configuration at any eccentricity by appropriately tuning Ma , which is otherwise not possible in isothermal flows. As $|Ma|$ decreases, the equilibrium position becomes increasingly eccentric, until a lower bound of $|Ma|$ is reached, for which the fixed point is located at $\Delta z > 1$ and hence is physically not possible. This lower bound of Ma strongly depends on the size of the inner drop.

Mathematically, Eq. (22) may be expanded in a Taylor series around $\Delta z = 0$ and reads $d(\Delta z)/dt = -C_0(Ma_c - Ma) - C_2(\Delta z)^2 + O(\Delta z^4)$, where C_0 and C_2 are positive constants that depend on Λ and the coefficient of Δz must be zero, on account of symmetry of the curves in panel (b). It is worth noting here that in the context of nonlinear dynamics [59], saddle-node bifurcation is defined as the process of creating a pair of equilibrium points (or fixed points), one of them stable and the other one unstable, when a system parameter (here, Ma) is varied beyond a critical value (here, $Ma > Ma_c$). When the said parameter is below the critical limit (i.e., when $Ma < Ma_c$), no equilibrium points exist. Based on the above definition, it becomes evident that the two equilibrium configurations here are created through a prototypical saddle-node bifurcation, when $Ma = Ma_c = -0.1168$. Interestingly, although a handful of previous studies [12,52,56] have also noted the presence of multiple possible equilibrium configurations, mainly for movement in quiescent fluids, it seems that this simple fact that the fixed points come about through a saddle-node bifurcation has never been reported.

Physically, the existence of stable fixed points implies that from any given initial position, the inner drop will eventually migrate toward the designated point and afterward both the drops will move with the same velocity. This migration has been demonstrated in Fig. 7(c), where the temporal evolution of $e(t)$ has been plotted, subject to an initial eccentricity: $e(t = 0) = 0$, for three different choices of $Ma = -0.1, -0.07$, and -0.03 , having stable fixed points at $e = 0.38, 0.6$, and 0.78 respectively. Motion of the inner drop toward the respective equilibrium configuration becomes clear from this figure, by observing that e becomes stagnant after a sufficiently long time. Further note that irrespective of Ma and the exact value of final e , the inner drop takes almost the same amount of time to reach its equilibrium position.

D. Deformation characteristics of the drops

The deformations given in the Eqs. (31) and (32) may be used to compute the shapes of the deformed outer and inner drops. The extent of this deformation can be quantified using the aspect ratio (\mathcal{AR}), defined as [67]

$$\mathcal{AR}_o = \frac{2\rho_{\max}^{(o)}}{H_v^{(o)}} \quad \text{for outer drop;} \quad \mathcal{AR}_I = \frac{2\rho_{\max}^{(I)}}{H_v^{(I)}} \quad \text{for inner drop.} \quad (34)$$

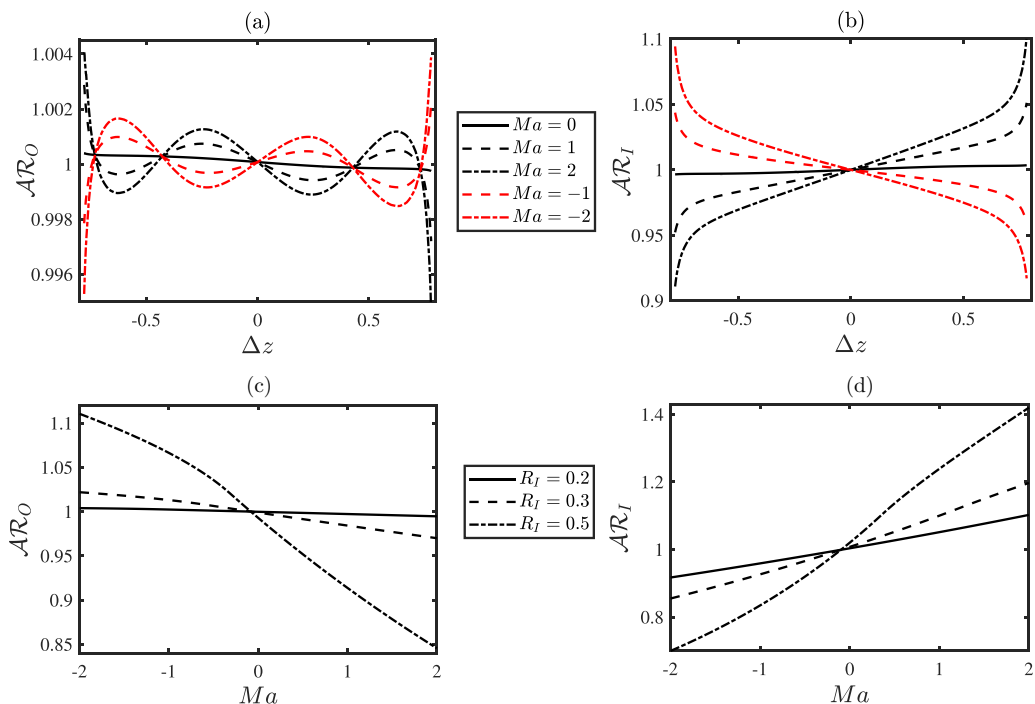


FIG. 8. Variation of \mathcal{AR}_O in panel (a) and of \mathcal{AR}_I in panel (b) as a function of Δz , for $Ma = 0, \pm 1$, and ± 2 and $R_I = 0.2$. (c) Plot of \mathcal{AR}_O vs Ma and (d) \mathcal{AR}_I vs Ma , for different inner drop sizes: $R_I = 0.2, 0.3$, and 0.5 , at the extreme respective eccentricities, $\Delta z = 0.78, 0.68$, and 0.48 . Other relevant parameters are $R = 5$, $\lambda_2 = 0.2, \lambda_3 = 1, \kappa_2 = 3, \kappa_3 = 1, Ca = 0.4$.

In Eq. (34), $2\rho_{\max}$ is the maximum width of a drop and H_v is the length of the drop along the centerline (i.e., $\rho = 0$, in Fig. 2). Therefore, the above equations essentially indicate whether the drop is stretched ($\mathcal{AR} < 1$) or squashed ($\mathcal{AR} > 1$) along the z_c axis. One can get further insight into the drop deformation by investigating the variations in the normal stresses across the interface, which mainly cause it to deform in the first place; see Eq. (23). At interface S_{ij} , this stress difference may be defined as [67]

$$\Delta T_{\xi\xi}^{(ij)} = \lambda_i p_i - \lambda_j p_j + \lambda_j \tau_{\xi\xi}^{(j)} - \lambda_i \tau_{\xi\xi}^{(i)}. \quad (35)$$

It may be inferred that $\Delta T_{\xi\xi}^{(12)}$ quantifies the difference between the stresses exerted by fluids 1 (outermost fluid) and 2 (outer drop), at the interface S_{12} . $\Delta T_{\xi\xi}^{(23)}$ may also be interpreted in the same way. The magnitude of $\Delta T_{\xi\xi}^{(ij)}$ governs the interfacial curvature. For the interface to remain spherical, $\Delta T_{\xi\xi}^{(ij)}$ has to be uniform along the interface.

Figures 8(a) and 8(b) exhibit how the aspect ratio (\mathcal{AR}) varies for the outer and the inner drops, when the eccentricity (Δz) of the inner core is varied, for different choices of $Ma = 0, \pm 1$, and ± 2 , while the inner drop radius has been chosen as $R_I = 0.2$. Figures 8(c) and 8(d), on the other hand, demonstrate the variations in \mathcal{AR} 's of the two drops as a function of Ma , for different sizes of the inner drop, $R_I = 0.2, 0.3$, and 0.5 . For every choice of R_I , the inner drops are located close to their respective extreme positions, given by $\Delta z = 0.78, 0.68$, and 0.48 respectively. All other relevant parameters are mentioned in the caption.

From panels (a) and (b) we observe that the deformations in both the drops attain maximum values, when the configuration is extremely eccentric, regardless of Ma . The deformation is extremely small for the outer drop, even when $Ca = 0.4$, which reaffirms our earlier assumption of

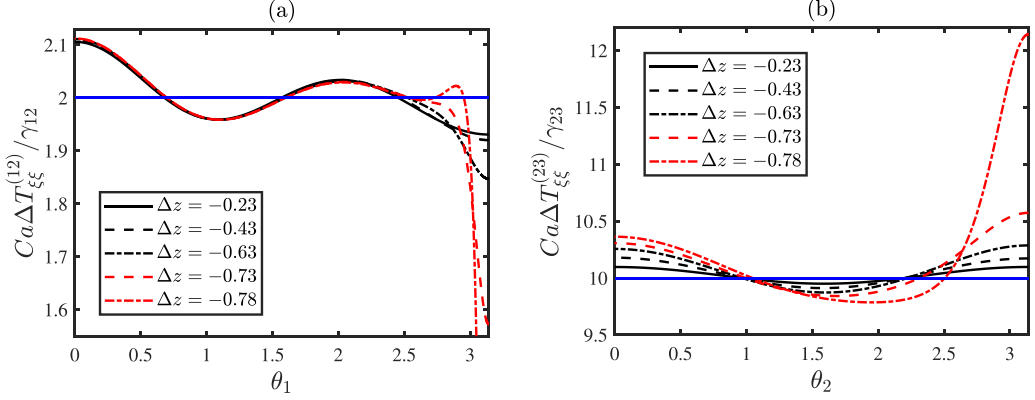


FIG. 9. Curvature of the outer drop ($\nabla \cdot \hat{\mathbf{n}}_{12}$) in (a) and the inner drop ($\nabla \cdot \hat{\mathbf{n}}_{23}$) in (b) vs the respective polar angles θ_1 and θ_2 , for various positions of the inner drop, $\Delta z = -0.23, -0.43, -0.63, -0.73$, and -0.78 . Constant curvatures are represented by solid blue lines. Other relevant parameters are $R_I = 0.2, R = 5, \lambda_2 = 0.2, \lambda_3 = 1, \kappa_2 = 3, \kappa_3 = 1, Ca = 0.4, Ma = 1$.

approximately spherical drops; also see Sec. S2 in the Supplemental Material [62]. For the inner drop as well, the shape does not deviate more than 10% from a sphere, which is in line with the asymptotic analysis carried out in Sec. IV. Notice that the deformation depends on whether the drops are in upstream or downstream configuration, as stated in relation to Fig. 5. Since the surface tension itself changes depending on the type of configuration, the interfaces deform accordingly. Notice that for both the drops, the deformation characteristics in the two configurations are essentially mirror images of each other. That is, if for a given eccentricity, the outer drop is stretched along the axis in, say, the upstream configuration, then it will be squashed axially for the same eccentricity in the downstream configuration. Although the deformation of the outer drop is extremely small, it still shows a fascinating nonmonotonic variation, depending on the position of the inner drop. Starting with concentric configuration with $\mathcal{AR}_O \approx 1$ and $Ma = 1 > 0$, when the inner core moves forward [$\Delta z > 0$; see the black curves in Fig. 8(a)] relative to the outer drop center, it naturally tends to exert an axial force on the outer drop, which stretches the same along the z axis and results in $\mathcal{AR}_O < 1$ for small values of eccentricity ($e < 0.23$). However, as e increases, U_3 decreases [see Fig. 4(d)] when $Ma > 0$ and hence the extent of deformation of the outer drop reduces, resulting in \mathcal{AR}_O going back up again. For an intermediate range of eccentricity ($0.43 < e < 0.73$) the axial force on the outer drop diminishes because the inner core slows down, which reverses the deformation trend as the drop is now squashed axially ($\mathcal{AR}_O > 1$). Finally, for very large eccentricities ($e > 0.73$), the presence of the inner core very close to the outer interface changes the stress distribution there along with the local temperature, which alters the surface tension. This again pushes the outer interface axially forward and hence results in $\mathcal{AR}_O < 1$ and axial stretching of the outer drop. When $Ma < 0$ or $\Delta z < 0$, the effects mentioned above are reversed and hence the deformation characteristics would follow the opposite pattern, as is clear from Fig. 8(a).

The deformation of the inner core [see Fig. 8(b)] is however monotonic in nature as it continuously increases with increasing eccentricity, regardless of Ma . When $Ma > 0$, the shape of the inner drop changes from prolate to oblate as it travels from an upstream toward a downstream configuration. The reverse is true when $Ma < 0$. The reason may be understood as follows. When $Ma = 1 > 0$ and the inner drop is at an extreme upstream location ($e = 0.78$), there will be a large jump in the normal stresses across its interface, especially at its rear end ($\theta_2 = \pi$); also see Fig. 9(b). This would result in larger curvature changes which extends the drop along the axial direction, leading to $\mathcal{AR}_I < 1$. As the drop travels toward the center of the outer drop (e or $|\Delta z|$ decreasing), its velocity increases, while the normal stress jump across its interface becomes less pronounced leading to a decrease in the extent of deformation and thus \mathcal{AR}_I inches towards 1. The opposite trend

is observed in the downstream configuration, when $\Delta z > 0$, simply because the effects mentioned above are reversed. Panels (a) and (b) further reveal that a larger imposed temperature gradient, characterized by a larger Ma , increases the deformation in both the drops. On the other hand, in an isothermal flow ($Ma = 0$), neither drop shows appreciable deformation, even when the capillary number is as large as 0.4.

Panels 8(c) and 8(d) delineate the effect of inner drop size on the deformation in a downstream configuration with near-maximum eccentricities. For instance, when $R_I = 0.5$, the maximum possible value of e is 0.5 and accordingly the curve representing $R_I = 0.5$ has been plotted for $e = 0.48$. The change of shape from prolate ($\mathcal{AR} < 1$) to oblate ($\mathcal{AR} > 1$) upon changing Ma is in exact agreement with panels 8(a) and 8(b). However, we observe that the minimum deformation ($\mathcal{AR} = 1$) does not occur at $Ma = 0$ for either drops. Rather, the outer drop witnesses minimum deformation when $Ma = -0.08$ and for the inner drop this value is $Ma = -0.1$. We reiterate that $\mathcal{AR} = 1$ means that the drops remain spherical. Essentially, at the Ma values mentioned above, the Marangoni stresses counteract the stress jump caused by the imposed background flow, as a result of which the deformation vanishes. Further note that an increase in the inner drop size always leads to larger deformation in both the drops. This is simply because a larger inner drop (especially one which is more viscous) would exert larger viscous stresses, which will naturally increase the deformation.

The nature of the deformations can be better understood by exploring the variation of interfacial curvature, which is governed by the normal stress difference across the interface, as mentioned in Eq. (35). In fact, the curvature and the stress jump across the interface are related as $\nabla \cdot \hat{\mathbf{n}}_{ij} = Ca \Delta T_{\xi\xi}^{(ij)} / \gamma_{ij}$. This quantity has been plotted in Figs. 9(a) and 9(b) for both the drops [in panel (a) for the outer drop and panel (b) for the inner drop], as a function of the respective polar angles θ_1 and θ_2 , for different inner drop positions, given by $\Delta z = -0.23, -0.43, -0.63, -0.73, -0.78$ (upstream configuration). Notice that the first four of these are the locations where \mathcal{AR}_O either changes sign or goes through a local maxima/minima [see Fig. 8(a)]. The straight blue lines in both panels indicate the stress jump required to maintain a uniform curvature, i.e., a spherical surface. When the stress jump is lower than this limit, the curvature is smaller, indicating that the drop surface becomes flatter. Note that in both the drops the maximum deviation in the stress jump (as compared to a spherical interface) occurs at the rear end ($\theta = \pi$), i.e., where the drop interfaces are closest to each other. As the inner drop approaches the outer interface, it squeezes out the fluid residing between the two surfaces, which leads to a large stress jump across both the interfaces. Further notice that the deviations from the uniform state (blue lines) has opposite signs for the two drops, signaling that they witness opposite kinds of deformation and is in perfect agreement with the previous figure. From panel (a), we observe that apart from the rear end ($\theta_1 = \pi$), the stress jump across the outer interface barely changes with eccentricity, which explains why deformation of the outer drop also changes so little with Δz .

Panel 9(b) on the other hand demonstrates that the normal stress jump across the inner drop surface deviates more from its base value (the blue line), as the eccentricity increases. As a result, its deformation increases with eccentricity. Observe that the inner drop experiences a positive curvature change at both the ends ($\theta_2 = 0$ and π), which indicates that the drop should be axially elongated for the particular choice of $Ma = 1$ and hence $\mathcal{AR}_I < 1$. This is again in exact agreement with the previous figure; see Fig. 8(b).

We end this section by visually exploring the drop shapes at different eccentricities, as shown in Figs. 10(a) and 10(b). Here we demonstrate how the shape of the inner drop changes as it travels within the outer drop (solid red line), whose center has been held fixed. In panel (a), we have chosen $Ma = 1 > 0$ and in panel (b) $Ma = -1 < 0$ has been taken. Since the outer drop barely deforms, its shape change is imperceptible and has not been represented here. On the other hand, to make the deformation of the inner drop legible, we have deliberately chosen $Ca = 0.6$, which, strictly speaking might be outside the range of validity of a leading-order analysis. As discussed earlier, when $Ma > 0$, the inner drop moves faster than the outer drop (see Fig. 7) and starting at $\Delta z < 0$, its shape slowly changes from prolate to oblate throughout the course of its motion; see panel (a).

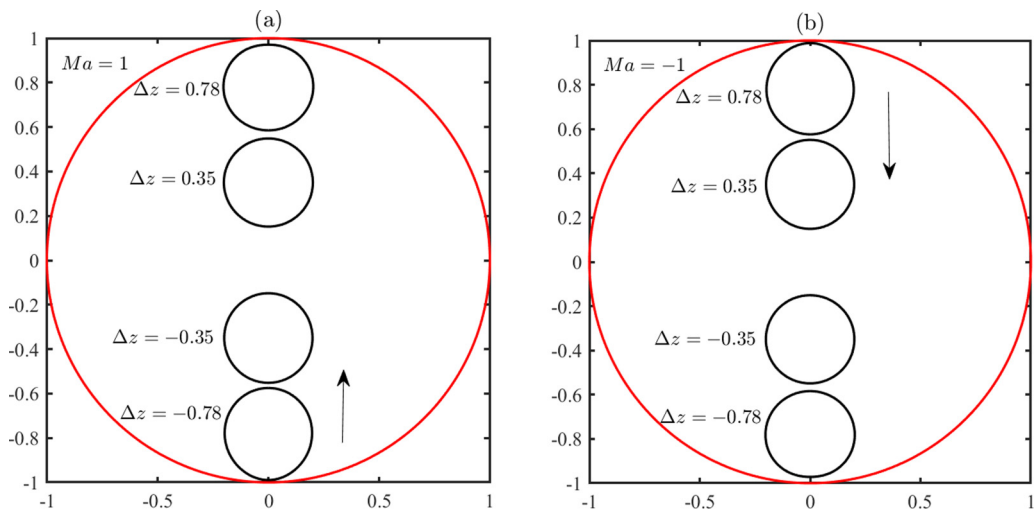


FIG. 10. Shape of the inner drop as it travels within the outer drop for $Ma = 1$ in (a) and $Ma = -1$ in (b). The solid red line represents the undeformed outer drop and the direction of relative movement has been shown with an arrow in each panel. Other relevant parameters are $R_I = 0.2$, $R = 5$, $\lambda_2 = 0.2$, $\lambda_3 = 1$, $\kappa_2 = 3$, $\kappa_3 = 1$, $Ca = 0.6$.

When $Ma = -1$, the outer drop moves faster and if the inner drop starts at a downstream position ($\Delta z > 0$) with a prolate shape, it will slowly become oblate, as it eventually trails the outer drop's center of mass.

VI. CONCLUSION

The effects of an externally imposed temperature gradient on the motion of a neutrally buoyant compound drop, suspended along the axis of a Poiseuille flow, have been analyzed here, wherein the surface tension varies linearly with temperature. In an effort to account for the naturally occurring eccentricity in such systems, bispherical coordinates are used to derive approximate semianalytical solutions, in the limit of small deformation [$Ca \ll O(1)$], employing asymptotic analysis. We also derive closed-form analytical solutions for the special case of concentric drops. We assume both energy and momentum transport to be diffusion-dominated and quasisteady, requiring that $Pe \ll O(1)$ and $Re \ll O(1)$. The resulting velocity and temperature fields are subsequently used to derive a closed-form expression for the leading-order [$O(Ca)$] deformation in both the drops. The analytical framework, especially for the deformations in eccentric compound drops, has hitherto not been reported in the literature. We have extensively validated our results for both droplet velocities and deformations in bispherical coordinates, by comparing them with previously reported studies in the literature as well as other known closed-form solutions.

A number of important conclusions can be drawn from our analysis. We establish that the velocities of both the drops may be either increased or decreased, depending on the magnitude and the direction of the imposed temperature gradient. Interestingly, the drop velocities do not depend on whether the inner core lies behind or ahead of the outer drop's center, while they are largely independent of the thermal properties of the inner core. The relative velocities of the two drops' centers of mass can also be finely tuned by imposing a temperature gradient. When $Ma > 0$, the inner drop always moves faster than the outer drop, while the opposite trend may be observed when $Ma < 0$. In fact, we demonstrate that by applying a temperature gradient below a critical threshold, it is possible to achieve a pair of equilibrium configurations at almost any eccentricity, where both the drops move at the same velocity. We further show that the upstream equilibrium configuration is

always unstable, while the downstream one is stable. Overall, the variations in the geometry (read, eccentricity) and the temperature gradient have a greater influence on the dynamics of the inner core.

Our analysis further demonstrates that the presence of external temperature gradients leads to larger deformations as compared to an isothermal flow and it strongly depends on Ma , size of the inner drop, its eccentricity, as well as the configuration (upstream or downstream). The deformation in the outer drop is negligibly small, while that of the inner drop strongly depends on the direction of the imposed temperature gradient and its position with respect to the outer drop's center of mass. For instance, we illustrate that for $Ma = -1$, when the inner core moves slower compared to the outer drop, its shape may change from being prolate to oblate as the configuration changes from downstream to upstream.

The framework developed here can also be used to study the motion of compound drops as well as drops or particles residing close to solid surfaces, with potential applications in biomedicine and separation processes.

ACKNOWLEDGMENTS

S.N.J. and U.G. gratefully acknowledge the financial support provided for this work by Science and Engineering Research Board (SERB), Government of India, through Ramanujan Research Grant No. SB/S2/RJN-180/2017.

APPENDIX: COMPLETE EQUATIONS FOR ECCENTRIC DROPS IN BISPHERICAL COORDINATES

1. Some useful identities

The following identities have been used to simplify and derive several equations in bispherical coordinates. Note that we have followed the sign convention for the upstream and downstream configurations as mentioned in Sec. IV.

$$\frac{1 - \zeta^2}{(\cosh \xi - \zeta)^{3/2}} = \sum_{n=0}^{\infty} 2\sqrt{2}n(n+1) e^{\mp(n+\frac{1}{2})\xi} C_{n+1}^{-\frac{1}{2}}(\zeta), \quad (\text{A1})$$

$$\frac{1 - \zeta^2}{(\cosh \xi - \zeta)^{1/2}} = \sum_{n=0}^{\infty} \frac{n(n+1)}{\sqrt{2}} \left[\frac{e^{\mp(n-\frac{1}{2})\xi}}{n-\frac{1}{2}} - \frac{e^{\mp(n+\frac{3}{2})\xi}}{n+\frac{3}{2}} \right] C_{n+1}^{-\frac{1}{2}}(\zeta), \quad (\text{A2})$$

$$\begin{aligned} \frac{(1 - \zeta^2)^2}{(\cosh \xi - \zeta)^{5/2}} &= \sum_{n=0}^{\infty} \frac{4\sqrt{2}n(n+1)}{3} \left[\frac{(n+2)(n+3)}{(2n+3)} e^{\mp(n+\frac{3}{2})\xi} \right. \\ &\quad \left. - \frac{(n-1)(n-2)}{(2n-1)} e^{\mp(n-\frac{1}{2})\xi} \right] C_{n+1}^{-\frac{1}{2}}(\zeta), \end{aligned} \quad (\text{A3})$$

$$\frac{\sinh \xi}{(\cosh \xi - \zeta)^{3/2}} = \pm \sum_{n=0}^{\infty} \sqrt{2}(2n+1) e^{\mp(n+\frac{1}{2})\xi} P_n(\zeta). \quad (\text{A4})$$

2. Linear system of algebraic equations for temperature and flow field

a. Algebraic equations for the temperature field

After substituting the expressions for χ_i from Eqs. (14) into the boundary conditions for temperature as given in Sec. IV B, the same may be simplified to derive linear algebraic equations for the unknown coefficients, a_n, b_n, \dots , etc., using the orthogonality property of the Gegenbauer polynomials. This orthogonality condition is given by [61]

$$\int_{-1}^1 \frac{C_{n+1}^{-\frac{1}{2}}(x)C_{k+1}^{-\frac{1}{2}}(x)}{1-x^2} dx = \frac{2\delta_{nk}}{n(n+1)(2n+1)}. \quad (\text{A5})$$

Since there are four unknown constants (a_n, c_n, d_n, e_n) , for every n , we get a set of $4N$ linear equations, given here (for $0 \leq n \leq N$):

$$[-a_{n-1} \mathcal{L}_{4n} + c_{n-1} \mathcal{L}_{5n} - d_{n-1} \mathcal{L}_{6n}](n+1) + a_n \mathcal{N}_{1n} - c_n \mathcal{N}_{2n} + d_n \mathcal{N}_{3n} + [-a_{n+1} \mathcal{L}_{7n} + c_{n+1} \mathcal{L}_{8n} - d_{n+1} \mathcal{L}_{9n}]n = 4S_n \mathcal{P}_{1n} \sinh \xi_1, \quad (\text{A6a})$$

$$-[c_{n-1} - d_{n-1} \pm e_{n-1}](n+1) + c_n \mathcal{N}_{4n} - d_n \mathcal{N}_{5n} \pm e_n \mathcal{N}_{5n} - [c_{n+1} - d_{n+1} \pm e_{n+1}]n = 0, \quad (\text{A6b})$$

$$-a_n \mathcal{L}_{1n} + c_n \kappa_2 \mathcal{L}_{2n} + d_n \kappa_2 \mathcal{L}_{3n} = S_n \mathcal{P}_{1n}, \quad (\text{A6c})$$

$$c_n \kappa_2 + d_n \kappa_2 - e_n \kappa_3 = 0, \quad (\text{A6d})$$

where

$$\mathcal{L}_{1n} = \sinh \left(n + \frac{1}{2} \right) \xi_1; \quad \mathcal{L}_{2n} = e^{(n+\frac{1}{2})(\xi_1-\xi_2)}; \quad \mathcal{L}_{3n} = e^{-(n+\frac{1}{2})(\xi_1-\xi_2)};$$

$$\mathcal{L}_{4n} = \cosh \left(n - \frac{1}{2} \right) \xi_1; \quad \mathcal{L}_{5n} = e^{(n-\frac{1}{2})(\xi_1-\xi_2)}; \quad \mathcal{L}_{6n} = e^{-(n-\frac{1}{2})(\xi_1-\xi_2)};$$

$$\mathcal{L}_{7n} = \cosh \left(n + \frac{3}{2} \right) \xi_1; \quad \mathcal{L}_{8n} = e^{(n+\frac{3}{2})(\xi_1-\xi_2)}; \quad \mathcal{L}_{9n} = e^{-(n+\frac{3}{2})(\xi_1-\xi_2)};$$

$$\mathcal{P}_{1n} = e^{\mp(n+\frac{1}{2})\xi_1}; \quad S_n = \sqrt{2n(n+1)}e^2;$$

$$\mathcal{N}_{1n} = (2n+1) \cosh \xi_1 \cosh \left(n + \frac{1}{2} \right) \xi_1 - \sinh \xi_1 \mathcal{L}_{1n};$$

$$\mathcal{N}_{2n} = [\cosh \xi_1 (2n+1) - \sinh \xi_1] \mathcal{L}_{2n}; \quad \mathcal{N}_{3n} = [\cosh \xi_1 (2n+1) + \sinh \xi_1] \mathcal{L}_{3n};$$

$$\mathcal{N}_{4n} = \cosh \xi_2 (2n+1) - \sinh \xi_2; \quad \mathcal{N}_{5n} = \cosh \xi_2 (2n+1) + \sinh \xi_2.$$

Note that in Eqs. (A6), the equation for the n th mode has coefficients from the $(n+1)$ th mode and thus we have to truncate the series after a certain number of terms (say, N), to compute the coefficients numerically. We observed that the series in Eqs. (14) are indeed convergent, although the truncation limit N for accurate solutions strongly depends on the value of eccentricity e . For example, when $R_l = 0.2$ and $0.001 \leq e < 0.6$, $N = 30$ is sufficient. However, for $0.6 \leq e \leq 0.78$ one has to take $N = 120$, to minimize truncation errors.

b. Shear stress in bispherical coordinates

The simplified shear stress $(\tau_{\xi\eta})$, upon using Eqs. (16), (17) along with the identities in Appendix A 1, may be written as

$$\tau_{\xi\eta}^{(i)} = -\frac{(\cosh \xi - \zeta)^{\frac{3}{2}}}{c^3 \sqrt{1 - \zeta^2}} \left[\sum_{n=0}^{\infty} \frac{d^2 W_n^{(i)}}{d\xi^2} C_{n+1}^{-\frac{1}{2}} + \frac{\delta_{j2} \delta_{k3}}{4\sqrt{2}} (U_3 - U_2) e^2 \sum_{n=0}^{\infty} n(n+1) \{ (2n-1) e^{\mp(n-\frac{1}{2})\xi} - (2n+3) e^{\mp(n+\frac{3}{2})\xi} \} C_{n+1}^{-\frac{1}{2}}(\zeta) \right]. \quad (\text{A7})$$

c. Algebraic equations for the flow field

The boundary conditions for velocity components in bispherical coordinates, as given in Sec. IV C, may be simplified to deduce a linear system of equations for the eight unknown constants $(A_n, B_n, E_n, F_n, G_n, H_n, \hat{C}_n, \hat{D}_n)$, for every n . These linear algebraic equations for the ‘‘upstream

configuration" ($\xi > 0$) are as follows:

$$A_n \mathcal{M}_n + B_n \hat{\mathcal{M}}_n = \hat{\mathcal{R}}_{1n} \left(\frac{\mathcal{K}_n \mathcal{Q}_n}{(2n-1)} - \frac{\hat{\mathcal{K}}_n \hat{\mathcal{Q}}_n}{(2n+3)} \right) - U_2 \hat{\mathcal{R}}_{1n} \left(\frac{\mathcal{Q}_n}{(2n-1)} - \frac{\hat{\mathcal{Q}}_n}{(2n+3)} \right), \quad (\text{A8a})$$

$$E_n \mathcal{M}_n + F_n \hat{\mathcal{M}}_n + G_n \mathcal{Q}_n + H_n \hat{\mathcal{Q}}_n = 0, \quad (\text{A8b})$$

$$(2n-1)\{(A_n - E_n)\mathcal{M}_n + G_n \mathcal{Q}_n\} + (2n+3)\{(B_n - F_n)\hat{\mathcal{M}}_n + H_n \hat{\mathcal{Q}}_n\} \\ = -\hat{\mathcal{R}}_{1n}(\mathcal{K}_n \mathcal{Q}_n - \hat{\mathcal{K}}_n \hat{\mathcal{Q}}_n) + U_2 \hat{\mathcal{R}}_{1n}(\mathcal{Q}_n - \hat{\mathcal{Q}}_n), \quad (\text{A8c})$$

$$(2n-1)^2\{(A_n - \lambda_2 E_n)\mathcal{M}_n - \lambda_2 G_n \mathcal{Q}_n\} + (2n+3)^2\{(B_n - \lambda_2 F_n)\hat{\mathcal{M}}_n - \lambda_2 H_n \hat{\mathcal{Q}}_n\} \\ = \left(\hat{\mathcal{R}}_{2n} \mathcal{J}_n - \hat{\mathcal{R}}_{3n} \sum_{k=0}^N \mathcal{J}_k \mathcal{U}_{n,k} + \hat{\mathcal{R}}_{1n} \{(2n-1)\mathcal{K}_n \mathcal{Q}_n - (2n+3)\hat{\mathcal{K}}_n \hat{\mathcal{Q}}_n\} \right) \\ - U_2 \hat{\mathcal{R}}_{1n} \{(2n-1)\mathcal{Q}_n - (2n+3)\hat{\mathcal{Q}}_n\}, \quad (\text{A8d})$$

$$E_n \mathcal{M}_n + F_n \hat{\mathcal{M}}_n + G_n \mathcal{Q}_n + H_n \hat{\mathcal{Q}}_n = (U_2 - U_3) \hat{\mathcal{R}}_{1n} \left(\frac{\mathcal{Q}_n}{(2n-1)} - \frac{\hat{\mathcal{Q}}_n}{(2n+3)} \right), \quad (\text{A8e})$$

$$\hat{\mathcal{C}}_n \mathcal{Q}_n + \hat{\mathcal{D}}_n \hat{\mathcal{Q}}_n = U_2 (\hat{\mathcal{R}}_{1n}) \left(\frac{\mathcal{Q}_n}{(2n-1)} - \frac{\hat{\mathcal{Q}}_n}{(2n+3)} \right) + U_3 \hat{\mathcal{R}}_{1n} \left(\frac{\mathcal{Q}_n}{(2n-1)} - \frac{\hat{\mathcal{Q}}_n}{(2n+3)} \right), \quad (\text{A8f})$$

$$(2n-1)\{E_n \mathcal{M}_n + (-G_n + \hat{\mathcal{C}}_n)\mathcal{Q}_n\} + (2n+3)\{F_n \hat{\mathcal{M}}_n + (-H_n + \hat{\mathcal{D}}_n)\hat{\mathcal{Q}}_n\} = 0, \quad (\text{A8g})$$

$$(2n-1)^2\{\lambda_2 E_n \mathcal{M}_n + (\lambda_2 G_n - \lambda_3 \hat{\mathcal{C}}_n)\mathcal{Q}_n\} + (2n+3)^2\{\lambda_2 F_n \hat{\mathcal{M}}_n + (\lambda_2 H_n - \lambda_3 \hat{\mathcal{D}}_n)\hat{\mathcal{Q}}_n\} \\ = \beta \left(\hat{\mathcal{R}}_{2n} \hat{\mathcal{J}}_n - \hat{\mathcal{R}}_{3n} \sum_{k=0}^N \hat{\mathcal{J}}_k \mathcal{U}_{n,k} \right) + U_2 (\lambda_2 - \lambda_3) \hat{\mathcal{R}}_{1n} \{(2n-1)\mathcal{Q}_n - (2n+3)\hat{\mathcal{Q}}_n\} \\ - U_3 (\lambda_2 - \lambda_3) \hat{\mathcal{R}}_{1n} \{(2n-1)\mathcal{Q}_n - (2n+3)\hat{\mathcal{Q}}_n\}. \quad (\text{A8h})$$

Note that Eqs. (A8a)–(A8d) are evaluated at $\xi = \xi_1$ and Eqs. (A8e)–(A8h) are evaluated at $\xi = \xi_2$. Following notations have been used in Eqs. (A8):

$$\mathcal{M}_n = e^{(n-\frac{1}{2})\xi}, \quad \hat{\mathcal{M}}_n = e^{(n+\frac{3}{2})\xi}, \quad \mathcal{Q}_n = e^{-(n-\frac{1}{2})\xi}, \quad \hat{\mathcal{Q}}_n = e^{-(n+\frac{3}{2})\xi}, \\ \hat{\mathcal{R}}_{1n} = n(n+1)c^2/\sqrt{2}, \quad \hat{\mathcal{R}}_{2n} = 2Ma c (2n+1), \quad \hat{\mathcal{R}}_{3n} = Ma c \sinh \xi n(n+1)(2n+1), \\ \mathcal{K}_n = \left(1 + \frac{2c^2}{3R^2} (n-1)(n-2) \right), \quad \hat{\mathcal{K}}_n = \left(1 + \frac{2c^2}{3R^2} (n+2)(n+3) \right), \\ \mathcal{J}_n = (c_n e^{(n+\frac{1}{2})(\xi_1-\xi_2)} + d_n e^{-(n+\frac{1}{2})(\xi_1-\xi_2)}), \quad \hat{\mathcal{J}}_n = c_n - d_n, \\ \mathcal{U}_{n,k}(\xi) = \int_{-1}^1 \frac{C_{n+1}^{-\frac{1}{2}}(x) C_{k+1}^{-\frac{1}{2}}(x)}{(\cosh \xi - x)(1-x^2)} dx.$$

Notice that the summation terms on the right-hand sides of Eqs. (A8d) and (A8h) are evaluated from the temperature field and thus can be truncated at the same N , as discussed earlier. Interestingly, in Eqs. (A8), unlike the temperature field, for every n , only the coefficients corresponding to that particular mode appear and hence these sets of equations may be solved exactly. For simplicity, we choose the number of modes for the flow field the same as N . In addition, recall that to compute the deformations (see Sec. IV E), one again has to truncate the series after a certain number of terms.

From the above equations, we can see that just like A_n in Sec. IV D 1, all other coefficients may also be written as a linear combination of U_2 and U_3 . For completeness, we show two examples here, while the rest of the coefficients follow the same pattern:

$$B_n = \mathcal{Y}_1^{(2)}(\mathbf{A}, e(t); n) + \mathcal{Y}_2^{(2)}(\mathbf{A}, e(t); n)U_2 + \mathcal{Y}_3^{(2)}(\mathbf{A}, e(t); n)U_3, \\ C_n = \mathcal{Y}_1^{(3)}(\mathbf{A}, e(t); n) + \mathcal{Y}_2^{(3)}(\mathbf{A}, e(t); n)U_2 + \mathcal{Y}_3^{(3)}(\mathbf{A}, e(t); n)U_3, \quad \text{etc.}$$

A similar system of linear algebraic equations to those in Eq. (A8) may also be deduced for the “downstream configuration” ($\xi < 0$), by choosing the correct signs of ξ . We do not mention them here explicitly to avoid repetition.

3. Complete relations for evaluating the deformation

a. Form of $\mathcal{E}^2\Psi$

The expression for $\mathcal{E}^2\Psi_i$ may be evaluated from the following:

$$\mathcal{E}^2\Psi_i = \frac{\sqrt{(\cosh \xi - \zeta)}}{c^2} \sum_{n=0}^{\infty} \left[C_{n+1}^{-\frac{1}{2}}(\zeta) \left\{ \frac{d^2 W_n^{(i)}}{d\xi^2} - \frac{2 \sinh \xi}{(\cosh \xi - \zeta)} \frac{dW_n^{(i)}}{d\xi} \right. \right. \\ \left. \left. + \frac{3(\cosh \xi + 3\zeta)}{4(\cosh \xi - \zeta)} W_n^{(i)} \right\} + (1 - \zeta^2) W_n^{(i)} \left\{ \frac{d^2 C_{n+1}^{-\frac{1}{2}}}{d\zeta^2} + \frac{2}{(\cosh \xi - \zeta)} \frac{dC_{n+1}^{-\frac{1}{2}}}{d\zeta} \right\} \right]. \quad (\text{A9})$$

Using the expressions for $W_n^{(i)}$ given in (20) and the recurrence relations for the Gegenbauer polynomials, the above equation may be simplified for the i th fluid as follows [67,68]:

$$\mathcal{E}^2\Psi_1 = \frac{1}{c^2 \sqrt{(\cosh \xi - \zeta)}} \sum_{n=0}^{\infty} [\bar{a}_n e^{\pm(n+\frac{1}{2})\xi} + \bar{c}_n e^{\mp(n+\frac{1}{2})\xi}] C_{n+1}^{-\frac{1}{2}}(\zeta), \quad (\text{A10})$$

$$\mathcal{E}^2\Psi_2 = \frac{1}{c^2 \sqrt{(\cosh \xi - \zeta)}} \sum_{n=0}^{\infty} [\bar{e}_n e^{\pm(n+\frac{1}{2})\xi} + \bar{g}_n e^{\mp(n+\frac{1}{2})\xi}] C_{n+1}^{-\frac{1}{2}}(\zeta), \quad (\text{A11})$$

$$\mathcal{E}^2\Psi_3 = \frac{1}{c^2 \sqrt{(\cosh \xi - \zeta)}} \sum_{n=0}^{\infty} \hat{c}_n e^{\mp(n+\frac{1}{2})\xi} C_{n+1}^{-\frac{1}{2}}(\zeta), \quad (\text{A12})$$

where

$$\bar{a}_n = -(2n-1)A_n + (2n+3)B_n + 2nA_{n+1} - 2(n+1)B_{n-1},$$

$$\bar{c}_n = -(2n-1)\bar{c}_n + (2n+3)\bar{d}_n + 2n\bar{c}_{n+1} - 2(n+1)\bar{d}_{n-1},$$

$$\bar{e}_n = -(2n-1)E_n + (2n+3)F_n + 2nE_{n+1} - 2(n+1)F_{n-1},$$

$$\bar{g}_n = -(2n-1)G_n + (2n+3)H_n + 2nG_{n+1} - 2(n+1)H_{n-1},$$

$$\hat{c}_n = -(2n-1)\hat{C}_n + (2n+3)\hat{D}_n + 2n\hat{C}_{n+1} - 2(n+1)\hat{D}_{n-1}.$$

b. The coefficients in the expressions for pressure

Substituting (29) for p_i and (A10) for $\mathcal{E}^2\Psi_i$ in Eqs. (26), we can deduce the relations between the two sets of coefficients, namely $\alpha_n^{(i)}$, $\beta_n^{(i)}$ and \bar{a}_n , \bar{c}_n , \dots , etc. These relations are given by [67,68]

$$\alpha_n^{(1)} = \alpha_0^{(1)} \pm \left[\sum_{m=1}^{n-1} \frac{\bar{a}_m}{m(m+1)} + \frac{\bar{a}_n}{n} \right], \quad \beta_n^{(1)} = \beta_0^{(1)} \pm (2n+1)\mathcal{F} \mp \left[\sum_{m=1}^{n-1} \frac{\bar{c}_m}{m(m+1)} + \frac{\bar{c}_n}{n} \right], \quad (\text{A13a})$$

$$\alpha_n^{(2)} = \alpha_0^{(2)} \pm \left[\sum_{m=1}^{n-1} \frac{\bar{e}_m}{m(m+1)} + \frac{\bar{e}_n}{n} \right], \quad \beta_n^{(2)} = \beta_0^{(2)} \pm (2n+1)\mathcal{F} \mp \left[\sum_{m=1}^{n-1} \frac{\bar{g}_m}{m(m+1)} + \frac{\bar{g}_n}{n} \right], \quad (\text{A13b})$$

$$\beta_n^{(3)} = \beta_0^{(3)} \pm (2n+1)\mathcal{F} \mp \left[\sum_{m=1}^{n-1} \frac{\hat{c}_m}{m(m+1)} + \frac{\hat{c}_n}{n} \right]. \quad (\text{A13c})$$

In Eqs. (A13), $\alpha_0^{(i)}$, $\beta_0^{(i)}$, \dots may be computed from the fact that the disturbance pressure ($p_i^{(d)}$), as given in Eq. (28), should vanish far away from the compound drop, i.e., as $\xi \rightarrow 0$. This condition yields [67,68]

$$\alpha_0^{(1)} = \mp \lim_{n \rightarrow \infty} \left[\sum_{m=1}^{n-1} \frac{\bar{a}_m}{m(m+1)} + \frac{\bar{a}_n}{n} \right] \text{ and } \beta_0^{(1)} = \mp \mathcal{F}, \quad (\text{A14})$$

$$\alpha_0^{(2)} = \mp \lim_{n \rightarrow \infty} \left[\sum_{m=1}^{n-1} \frac{\bar{e}_m}{m(m+1)} + \frac{\bar{e}_n}{n} \right] \text{ and } \beta_0^{(2)} = \beta_0^{(3)} = \mp \mathcal{F}. \quad (\text{A15})$$

c. Normal stress in bispherical coordinates

The expression for $\tau_{\xi\xi}$ may be simplified by using Eqs. (16), (17), along with the recursion relations and identities for the Gegenbauer and Legendre polynomials (see Appendix A1). In the i th fluid ($i = 1, 2, 3$), this expression reads

$$\begin{aligned} \tau_{\xi\xi}^{(i)} = & \frac{\sqrt{(\cosh \xi - \zeta)}}{c^3} \left[\sum_{n=0}^{\infty} \left(2 \cosh \xi \frac{dW_n^{(i)}}{d\xi} + \sinh \xi W_n^{(i)} \right) P_n(\zeta) - \sum_{n=1}^{\infty} \frac{dW_{n-1}^{(i)}}{d\xi} P_n(\zeta) \right. \\ & \left. - \sum_{n=0}^{\infty} \frac{dW_{n+1}^{(i)}}{d\xi} P_n(\zeta) - \frac{3\delta_{i2}\delta_{j3}}{2\sqrt{2}} (U_3 - U_2) c^2 \sum_{n=0}^{\infty} n(n+1) \left\{ \mp e^{\mp(n-\frac{1}{2})\xi} \pm e^{\mp(n+\frac{3}{2})\xi} \right\} C_{n+1}^{-\frac{1}{2}}(\zeta) \right]. \end{aligned} \quad (\text{A16})$$

d. Expressions for $\mathcal{G}_{ij}(\zeta)$ and $\hat{\mathcal{G}}_{ij}(\zeta)$

The expressions for $\mathcal{G}_{ij}(\zeta)$ and $\hat{\mathcal{G}}_{ij}(\zeta)$, appearing in Eq. (30), are as follows:

$$\hat{\mathcal{G}}_{12}(\zeta) = \frac{\pm c}{(1 - \zeta^2)(\cosh \xi_1 - \zeta)}, \quad \hat{\mathcal{G}}_{23}(\zeta) = \frac{\pm c}{\gamma(1 - \zeta^2)(\cosh \xi_2 - \zeta)}, \quad \mathcal{G}_{ij}(\zeta) = \mathcal{H}_{ij} \hat{\mathcal{G}}_{ij}(\zeta),$$

where

$$\begin{aligned} \mathcal{H}_{ij} = & \pm \frac{2\beta_{ij}\text{Ma} \sinh \xi T_{ij}}{c} + \frac{4h_O}{R^2} (\lambda_j - \lambda_i) + \frac{\sqrt{(\cosh \xi - \zeta)}}{c^3} \left[\sum_{n=0}^{\infty} \left\{ 2 \cosh \xi \left(\lambda_i \frac{dW_n^{(i)}}{d\xi} \right. \right. \right. \\ & \left. \left. - \lambda_j \frac{dW_n^{(j)}}{d\xi} \right) + \sinh \xi (\lambda_i W_n^{(i)} - \lambda_j W_n^{(j)}) \right\} P_n(\zeta) - \sum_{n=1}^{\infty} \left(\lambda_i \frac{dW_{n-1}^{(i)}}{d\xi} - \lambda_j \frac{dW_{n-1}^{(j)}}{d\xi} \right) P_n(\zeta) \\ & \left. - \sum_{n=0}^{\infty} \left(\lambda_i \frac{dW_{n+1}^{(i)}}{d\xi} - \lambda_j \frac{dW_{n+1}^{(j)}}{d\xi} \right) P_n(\zeta) - \frac{3\delta_{i2}\delta_{j3}}{2\sqrt{2}} (\lambda_2 - \lambda_3) (U_3 - U_2) c^2 \sum_{n=0}^{\infty} n(n+1) \right. \\ & \times \left\{ \mp e^{\mp(n-\frac{1}{2})\xi} \pm e^{\mp(n+\frac{3}{2})\xi} \right\} C_{n+1}^{-\frac{1}{2}} + \sum_{n=0}^{\infty} \left\{ (\lambda_j \alpha_n^{(j)} - \lambda_i \alpha_n^{(i)}) e^{\pm(n+\frac{1}{2})\xi} \right. \\ & \left. \left. + (\lambda_j \beta_n^{(j)} - \lambda_i \beta_n^{(i)}) e^{\mp(n+\frac{1}{2})\xi} \pm (\lambda_i - \lambda_j) F(2n+1) e^{\mp(n+\frac{1}{2})\xi} \right\} P_n(\zeta) \right]_{S_{ij}}. \end{aligned} \quad (\text{A17})$$

Note that in Eq. (A17), \mathcal{H}_{ij} is evaluated on the surface S_{ij} and the following notations are considered: $\lambda_1 = 1$, $\beta_{12} = 1$, and $\beta_{23} = \beta$.

- [1] A. S. Utada, E. Lorenceau, D. R. Link, P. D. Kaplan, H. A. Stone, and D. Weitz, Monodisperse double emulsions generated from a microcapillary device, *Science* **308**, 537 (2005).
- [2] A. R. Abate, J. Thiele, and D. A. Weitz, One-step formation of multiple emulsions in microfluidics, *Lab Chip* **11**, 253 (2011).
- [3] E. Dickinson, Double emulsions stabilized by food biopolymers, *Food Biophys.* **6**, 1 (2011).
- [4] H. Lamba, K. Sathish, and L. Sabikhi, Double emulsions: Emerging delivery system for plant bioactives, *Food Bioprocess Technol.* **8**, 709 (2015).
- [5] Y. Zhang, H. F. Chan, and K. W. Leong, Advanced materials and processing for drug delivery: The past and the future, *Adv. Drug Delivery Rev.* **65**, 104 (2013).
- [6] M. Iqbal, N. Zafar, H. Fessi, and A. Elaissari, Double emulsion solvent evaporation techniques used for drug encapsulation, *Int. J. Pharm.* **496**, 173 (2015).
- [7] H.-C. Kan, H. Udaykumar, W. Shyy, and R. Tran-Son-Tay, Hydrodynamics of a compound drop with application to leukocyte modeling, *Phys. Fluids* **10**, 760 (1998).
- [8] C. Lim, E. Zhou, and S. Quek, Mechanical models for living cells: A review, *J. Biomech.* **39**, 195 (2006).
- [9] J. Draxler and R. Marr, Emulsion liquid membranes. Part I: Phenomenon and industrial application, *Chemical Engineering and Processing: Process Intensification* **20**, 319 (1986).
- [10] S. Santra, D. P. Panigrahi, S. Das, and S. Chakraborty, Shape evolution of compound droplet in combined presence of electric field and extensional flow, *Phys. Rev. Fluids* **5**, 063602 (2020).
- [11] E. Rushton and G. Davies, Settling of encapsulated droplets at low Reynolds numbers, *Int. J. Multiphase Flow* **9**, 337 (1983).
- [12] S. Sadhal and H. Oguz, Stokes flow past compound multiphase drops: The case of completely engulfed drops/bubbles, *J. Fluid Mech.* **160**, 511 (1985).
- [13] R. E. Johnson and S. Sadhal, Stokes flow past bubbles and drops partially coated with thin films. Part 2. Thin films with internal circulation: A perturbation solution, *J. Fluid Mech.* **132**, 295 (1983).
- [14] H. Stone and L. Leal, Breakup of concentric double emulsion droplets in linear flows, *J. Fluid Mech.* **211**, 123 (1990).
- [15] K. A. Smith, J. M. Ottino, and M. Olvera de la Cruz, Encapsulated Drop Breakup in Shear Flow, *Phys. Rev. Lett.* **93**, 204501 (2004).
- [16] S. Kim and S. Dabiri, Transient dynamics of eccentric double emulsion droplets in a simple shear flow, *Phys. Rev. Fluids* **2**, 104305 (2017).
- [17] S. Santra, S. Das, and S. Chakraborty, Electrically modulated dynamics of a compound droplet in a confined microfluidic environment, *J. Fluid Mech.* **882**, A23 (2020).
- [18] S.-L. Chiu and T.-H. Lin, Experiment on the dynamics of a compound drop impinging on a hot surface, *Phys. Fluids* **17**, 122103 (2005).
- [19] S. Zhu, A. Kherbeche, Y. Feng, and M.-J. Thoraval, Impact of an air-in-liquid compound drop onto a liquid surface, *Phys. Fluids* **32**, 041705 (2020).
- [20] S. Mortazavi and G. Tryggvason, A numerical study of the motion of drops in Poiseuille flow. Part 1. Lateral migration of one drop, *J. Fluid Mech.* **411**, 325 (2000).
- [21] J. T. Schwalbe, F. R. Phelan Jr., P. M. Vlahovska, and S. D. Hudson, Interfacial effects on droplet dynamics in Poiseuille flow, *Soft Matter* **7**, 7797 (2011).
- [22] O. Aouane, A. Farutin, M. Thiébaud, A. Benyoussef, C. Wagner, and C. Misbah, Hydrodynamic pairing of soft particles in a confined flow, *Phys. Rev. Fluids* **2**, 063102 (2017).
- [23] S. Das and S. Chakraborty, Thermally modulated cross-stream migration of a surfactant-laden deformable drop in a Poiseuille flow, *Phys. Rev. Fluids* **3**, 103602 (2018).
- [24] R. Pal, Pipeline flow of unstable and surfactant-stabilized emulsions, *AIChE J.* **39**, 1754 (1993).
- [25] B. Reichert, I. Cantat, and M.-C. Jullien, Predicting droplet velocity in a Hele-Shaw cell, *Phys. Rev. Fluids* **4**, 113602 (2019).
- [26] G. Danker, P. M. Vlahovska, and C. Misbah, Vesicles in Poiseuille Flow, *Phys. Rev. Lett.* **102**, 148102 (2009).
- [27] Q. M. Qi and E. S. G. Shaqfeh, Theory to predict particle migration and margination in the pressure-driven channel flow of blood, *Phys. Rev. Fluids* **2**, 093102 (2017).

- [28] S. Mandal, A. Bandopadhyay, and S. Chakraborty, The effect of uniform electric field on the cross-stream migration of a drop in plane Poiseuille flow, *J. Fluid Mech.* **809**, 726 (2016).
- [29] B. Nath, G. Biswas, A. Dalal, and K. C. Sahu, Cross-stream migration of drops suspended in Poiseuille flow in the presence of an electric field, *Phys. Rev. E* **97**, 063106 (2018).
- [30] S. Das, S. Mandal, S. Som, and S. Chakraborty, Migration of a surfactant-laden droplet in non-isothermal Poiseuille flow, *Phys. Fluids* **29**, 012002 (2017).
- [31] S. Das, S. Mandal, and S. Chakraborty, Effect of transverse temperature gradient on the migration of a deformable droplet in a Poiseuille flow, *J. Fluid Mech.* **850**, 1142 (2018).
- [32] O. S. Pak, J. Feng, and H. A. Stone, Viscous Marangoni migration of a drop in a Poiseuille flow at low surface Péclet numbers, *J. Fluid Mech.* **753**, 535 (2014).
- [33] J. A. Hanna and P. M. Vlahovska, Surfactant-induced migration of a spherical drop in Stokes flow, *Phys. Fluids* **22**, 013102 (2010).
- [34] S. Mandal, U. Ghosh, and S. Chakraborty, Effect of surfactant on motion and deformation of compound droplets in arbitrary unbounded Stokes flows, *J. Fluid Mech.* **803**, 200 (2016).
- [35] Y. Song, J. Xu, and Y. Yang, Stokes flow past a compound drop in a circular tube, *Phys. Fluids* **22**, 072003 (2010).
- [36] M. P. Borthakur, G. Biswas, and D. Bandyopadhyay, Dynamics of deformation and pinch-off of a migrating compound droplet in a tube, *Phys. Rev. E* **97**, 043112 (2018).
- [37] V. Thammanna Gurumurthy and S. Pushpavanam, Hydrodynamics of a compound drop in plane Poiseuille flow, *Phys. Fluids* **32**, 072003 (2020).
- [38] A. Borhan, H. Haj-Hariri, and A. Nadim, Effect of surfactants on the thermocapillary migration of a concentric compound drop, *J. Colloid Interface Sci.* **149**, 553 (1992).
- [39] J.-W. Ha and S.-M. Yang, Fluid dynamics of a double emulsion droplet in an electric field, *Phys. Fluids* **11**, 1029 (1999).
- [40] P. Soni, R. M. Thakkar, and V. A. Juvekar, Electrohydrodynamics of a concentric compound drop in an AC electric field, *Phys. Fluids* **30**, 032102 (2018).
- [41] J. T. Davies, *Interfacial Phenomena* (Elsevier, New York, 2012).
- [42] J. Won, W. Lee, and S. Song, Estimation of the thermocapillary force and its applications to precise droplet control on a microfluidic chip, *Sci. Rep.* **7**, 3062 (2017).
- [43] R. Balasubramaniam and A.-T. Chai, Thermocapillary migration of droplets: An exact solution for small Marangoni numbers, *J. Colloid Interface Sci.* **119**, 531 (1987).
- [44] B. R. Duffy, S. K. Wilson, J. J. A. Conn, and K. Sefiane, Unsteady motion of a long bubble or droplet in a self-wetting system, *Phys. Rev. Fluids* **3**, 123603 (2018).
- [45] S. K. Wilson, The steady thermocapillary-driven motion of a large droplet in a closed tube, *Phys. Fluids A* **5**, 2064 (1993).
- [46] S. K. Wilson, The effect of an axial temperature gradient on the steady motion of a large droplet in a tube, *J. Eng. Math.* **29**, 205 (1995).
- [47] V. Miralles, A. Huerre, H. Williams, B. Fournié, and M.-C. Jullien, A versatile technology for droplet-based microfluidics: Thermomechanical actuation, *Lab Chip* **15**, 2133 (2015).
- [48] A. Karbalaei, R. Kumar, and H. J. Cho, Thermocapillarity in microfluidics: A review, *Micromachines* **7**, 13 (2016).
- [49] R. S. Subramanian, Thermocapillary migration of bubbles and droplets, *Adv. Space Res.* **3**, 145 (1983).
- [50] R. Balasubramaniam, C. E. Lacy, G. Woniak, and R. S. Subramanian, Thermocapillary migration of bubbles and drops at moderate values of the Marangoni number in reduced gravity, *Phys. Fluids* **8**, 872 (1996).
- [51] O. Lavrenteva and A. Nir, *Advances in Multiphase Flow and Heat Transfer*, edited by L. Chen and D. Mewes, Vol. 1 (Bentham Science Publishers, Sharjah, 2009).
- [52] D. S. Morton, R. S. Subramanian, and R. Balasubramanian, The migration of a compound drop due to thermocapillarity, *Phys. Fluids A* **2**, 2119 (1990).
- [53] L. Rosenfeld, O. Lavrenteva, and A. Nir, On the thermocapillary motion of partially engulfed compound drops, *J. Fluid Mech.* **626**, 263 (2009).

- [54] O. M. Lavrenteva, L. Rosenfeld, and A. Nir, Shape change, engulfment, and breakup of partially engulfed compound drops undergoing thermocapillary migration, *Phys. Rev. E* **84**, 056323 (2011).
- [55] C. Laugel, A. Baillet, M. P. Y. Piemi, J. Marty, and D. Ferrier, Oil-water-oil multiple emulsions for prolonged delivery of hydrocortisone after topical application: Comparison with simple emulsions, *Int. J. Pharm.* **160**, 109 (1998).
- [56] H. Gouz and S. Sadhal, Fluid dynamics and stability analysis of a compound droplet in an electric field, *Q. J. Mech. Appl. Math.* **42**, 65 (1989).
- [57] H. Brenner, The slow motion of a sphere through a viscous fluid towards a plane surface, *Chem. Eng. Sci.* **16**, 242 (1961).
- [58] J. Happel and H. Brenner, *Low Reynolds Number Hydrodynamics: With Special Applications to Particulate Media*, Vol. 1 (Springer Science & Business Media, The Hague, 2012).
- [59] S. H. Strogatz, *Nonlinear Dynamics and Chaos: With Applications to Physics, Biology, Chemistry, and Engineering* (CRC Press, Boulder, 2001).
- [60] G. Hetsroni and S. Haber, The flow in and around a droplet or bubble submerged in an unbound arbitrary velocity field, *Rheol. Acta* **9**, 488 (1970).
- [61] L. G. Leal, *Advanced Transport Phenomena: Fluid Mechanics and Convective Transport Processes* (Cambridge University Press, Cambridge, 2007).
- [62] See Supplemental Material at <http://link.aps.org/supplemental/10.1103/PhysRevFluids.6.073602> for the details of motion and deformation of concentric compound drops.
- [63] S. S. Sadhal, A note on the thermocapillary migration of a bubble normal to a plane surface, *J. Colloid Interface Sci.* **95**, 283 (1983).
- [64] M. Stimson and G. B. Jeffery, The motion of two spheres in a viscous fluid, *Proc. R. Soc. London, Ser. A* **111**, 110 (1926).
- [65] G. B. Jeffery, On a form of the solution of Laplace's equation suitable for problems relating to two spheres, *Proc. R. Soc. London, Ser. A* **87**, 109 (1912).
- [66] E. Wacholder and D. Weihs, Slow motion of a fluid sphere in the vicinity of another sphere or a plane boundary, *Chem. Eng. Sci.* **27**, 1817 (1972).
- [67] S. N. Jadhav and U. Ghosh, Effect of surfactant on the settling of a drop towards a wall, *J. Fluid Mech.* **912**, A4 (2021).
- [68] E. Chervenivanova and Z. Zapryanov, On the deformation of two droplets in a quasisteady Stokes flow, *Int. J. Multiphase Flow* **11**, 721 (1985).
- [69] A. C. King, J. Billingham, and S. R. Otto, *Differential Equations: Linear, Nonlinear, Ordinary, Partial* (Cambridge University Press, Cambridge, 2003).
- [70] V. R. Patel, G. G. Dumancas, L. C. K. Viswanath, R. Maples, and B. J. J. Subong, Castor oil: Properties, uses, and optimization of processing parameters in commercial production, *Lipid Insights* **9**, 1 (2016).
- [71] J. R. Pound, LXX.—Interfacial tension, *J. Chem. Soc., Trans.* **123**, 578 (1923).
- [72] L. Saias, J. Autebert, L. Malaquin, and J.-L. Viovy, Design, modeling and characterization of microfluidic architectures for high flow rate, small footprint microfluidic systems, *Lab Chip* **11**, 822 (2011).
- [73] S. Biswas, J. T. Miller, Y. Li, K. Nandakumar, and C. S. Kumar, Developing a millifluidic platform for the synthesis of ultrasmall nanoclusters: Ultrasmall copper nanoclusters as a case study, *Small* **8**, 688 (2012).
- [74] G. Gittens, Variation of surface tension of water with temperature, *J. Colloid Interface Sci.* **30**, 406 (1969).
- [75] X. Qu and Y. Wang, Dynamics of concentric and eccentric compound droplets suspended in extensional flows, *Phys. Fluids* **24**, 123302 (2012).
- [76] K. D. Barton and R. S. Subramanian, Thermocapillary migration of a liquid drop normal to a plane surface, *J. Colloid Interface Sci.* **137**, 170 (1990).